HSV-1 exploits host heterochromatin for egress

Hannah C Lewis*[1,2], Laurel E Kelnhofer-Millevolte*[1,2,3], Mia R Brinkley[1], Hannah E Arbach[1], Edward A Arnold[1,4], Srinivas Ramachandran[5, 6, #], and Daphne C Avgousti[1,7,8, #]

1 Human Biology Division, Fred Hutchinson Cancer Research Center, 1100 Fairview Avenue North, Seattle, WA 98109

2 Molecular & Cellular Biology, Graduate Program, University of Washington and Fred Hutchinson Cancer Research Center, 1959 NE Pacific Street Box 357275 Seattle, WA 98195

3 UW Medical Scientist Training Program, 1959 NE Pacific Street Box 357470, Seattle, WA 98195

4 Microbiology Graduate Program, University of Washington, 1705 NE Pacific Street Box 357735, Seattle, WA 98195

5 RNA Bioscience Initiative, University of Colorado School of Medicine,

6 Department of Biochemistry and Molecular Genetics, University of Colorado School of Medicine, 12801 East 17th Avenue Mail Stop 8101, Aurora, CO 80045

7 Twitter: @avgousti_lab

8 Lead contact

* Authors contributed equally

Address correspondence to: srinivas.ramachandran@cuanschutz.edu (S.R.), avgousti@fredhutch.org (D.C.A.)

Abstract

Herpes simplex virus (HSV-1) progeny form in the nucleus and must exit to successfully infect other cells. These newly formed viral capsids navigate the complex chromatin architecture of the nucleus to reach the inner nuclear membrane and egress. Here, we demonstrate by transmission electron microscopy (TEM) that HSV-1 capsids traverse dense heterochromatin in the nuclear periphery to reach the inner nuclear membrane. We found that this heterochromatin is dependent on the specific chromatin marks of trimethylation on histone H3 lysine 27 (H3K27me3) and the histone variant macroH2A1. Through chromatin profiling over the course of infection, we revealed massive host genomic regions bound by macroH2A1 and H3K27me3 that correlate with decreased host transcription in active compartments. This indicates the formation of new heterochromatin during infection. We found that loss of these markers resulted in significantly lower viral titers but did not impact viral genome or protein accumulation. Strikingly, we discovered by TEM that loss of macroH2A1 or H3K27me3 resulted in nuclear trapping of viral capsids. Thus, our work demonstrates that HSV-1 takes advantage of the dynamic nature of host heterochromatin formation during infection for efficient viral egress.

INTRODUCTION

Nuclear replicating viruses must contend with host chromatin to establish a successful infection. Like most DNA viruses, herpes simplex virus (HSV-1) takes advantage of host chromatin factors both by incorporating histones onto its genome to promote gene expression[1] and by reorganizing host chromatin during infection[2–4]. This redistribution of host chromatin results in a global increase in heterochromatin[5]. Host chromatin that accumulates in the nuclear periphery during HSV-1 infection creates a potential barrier for capsids to egress from the nucleus. HSV-1 capsids egress by a unique mechanism of budding into the inner nuclear membrane and then fusing with the outer nuclear membrane for further maturation in the cytosol[6,7]. Viral capsids traversing this dense chromatin in the nuclear periphery are associated with channels of less dense staining, termed heterochromatin channels[8]. However, it is not known if these channels are necessary for viral egress and the mechanisms by which they form are unclear.

Heterochromatin density and subnuclear localization is affected by the presence and ratio of specific histone modifications. In uninfected cells, histone modifications such as trimethylation of histone H3 lysine 27 (H3K27me3) and the histone variant macroH2A1, among others, delineate heterochromatin regions that are largely localized to the nuclear periphery. H3K27me3 is deposited by the EZH2 enzyme[9], a member of the polycomb repressive complex (PRC2)[10]. This modification is bound by PRC2, leading to modification of adjacent nucleosomes, which results in formation of dense heterochromatin domains that repress transcription. MacroH2A, the largest of the histone variants, consists of a canonical histone fold domain, a small linker region and a C-terminal 25kDa macro domain that is thought to protrude from the nucleosome[11]. There are three isoforms referred to collectively as macroH2A: macroH2A1.1, macroH2A1.2 and macroH2A2. MacroH2A1.1 and macroH2A1.2 are splice variants of the same gene that differ by one exon resulting in a 28-amino acid difference in the macro domain. MacroH2A1 was found to be downregulated in melanoma[12], suggesting a key role in the maintenance of genome integrity. Importantly, loss of macroH2A1 and macroH2A2 results in a significant decrease in heterochromatin in the nuclear periphery observed by electron microscopy[13]. Furthermore, macroH2A1 also demarcates regions of host chromatin that associate with the nuclear lamina[14], termed lamina-associated domains (LADs), highlighting its importance in linking chromatin with the nuclear envelope to support nuclear integrity.

In this study, we visualized HSV-1 nuclear egress by transmission electron microscopy (TEM) and found that capsids reach the inner nuclear membrane in regions of less densely stained chromatin. Therefore, we hypothesized that HSV-1 exploits host heterochromatin to generate

77 channels and successfully egress from the nuclear compartment. We examined chromatin
78 structure by TEM in the absence of heterochromatin markers macroH2A1 and H3K27me3 and
79 discovered that peripheral heterochromatin is largely dependent on these marks. We used
80 chromatin profiling of macroH2A1 and H3K27me3 during HSV-1 infection to define the specific
81 host genomic regions bound by these markers and found that they demarcate broad regions of
82 heterochromatin that form in transcriptionally active compartments. Importantly, we found that
83 the loss of macroH2A1 results in significantly lower viral titers but does not impair viral
84 transcription, protein production, or replication in both lab adapted and clinical isolates of HSV-
85 1. Furthermore, by inhibiting EZH2 deposition of H3K27me3, we found that reduction of
86 H3K27me3 also leads to a significant decrease in viral titers. Finally, we determined by TEM
87 that loss of macroH2A1 or H3K27me3 results in significantly more viral capsids trapped in the
88 nuclear compartment, pinpointing the importance of heterochromatin in viral nuclear egress. Our
89 study is the first to demonstrate that HSV-1 infection manipulates heterochromatin markers to
90 successfully egress from the nuclear compartment.

91 **RESULTS**

92 **HSV-1 capsids associate with regions of less dense chromatin to escape the nucleus**

93 To investigate the journey of HSV-1 capsids to the inner nuclear membrane, we used
94 transmission electron microscopy (TEM) to image nuclei and examined heterochromatin
95 formation in human foreskin fibroblast (HFF) cells. HFF cells are used as a model for HSV-1
96 infection as they represent a common site of infection in humans[15]. In uninfected cells, we
97 observed the characteristic dark heterochromatin staining in the nuclear periphery (Fig 1a,
98 arrowhead). Upon infection with HSV-1, we observed capsids interacting with the inner nuclear
99 membrane primarily in regions of less dense staining (Fig 1b, arrows). These results are
100 consistent with previous reports in African green monkey kidney cells (Vero) and human B cells
101 where viral capsids were observed to interact with the inner nuclear membrane in regions of
102 less dense staining, or heterochromatin channels[8,16]. Because heterochromatin in the nuclear
103 periphery was dependent on macroH2A presence in hepatoma cells[13], and macroH2A1
104 commonly overlaps with H3K27me3[17], we chose to examine heterochromatin formation in the
105 absence of these markers in HFFs.

106

107 **Heterochromatin markers macroH2A1 and H3K27me3 are critical for heterochromatin**
108 **formation in the nuclear periphery**

109 We used CRISPR-Cas9 to knock-out (KO) expression of the *macroH2A1* gene in hTERT-
110 immortalized HFF cells (HFF-T) cells, which resulted in the loss of macroH2A1.1 and
111 macroH2A1.2, termed macroH2A1 KO cells. We found by TEM that macroH2A1 KO cells had
112 strikingly less heterochromatin in the nuclear periphery than WT cells (Fig 1c). We quantified the
113 width of heterochromatin at the nuclear periphery in each cell type through binary thresholding
114 of the intensity of electron-dense regions and found that loss of macroH2A1 results in a
115 significant reduction in peripheral heterochromatin (Fig 1e). To reduce H3K27me3 levels, we
116 targeted the EZH2 enzyme that deposits this mark[18] using a well-characterized inhibitor called
117 tazemetostat (EPZ-6438)[19]. We treated cells with 10 μM of tazemetostat or DMSO control for 3
118 days to allow for reduction of H3K27me3 and imaged nuclei by TEM (Fig 1d). Similar to
119 macroH2A1 KO cells, we found a significant decrease in heterochromatin in the nuclear
120 periphery of cells with depleted H3K27me3 (Fig 1e). It is important to note that in cells with
121 observed decreased heterochromatin that there is not a decrease in total chromatin. These cells
122 are simply not able to condense their chromatin to a degree that it would be visible by TEM.
123 Importantly, the genomic regions bound by macroH2A1 and H3K27me3 are sufficiently massive
124 that changes are visible by TEM. Therefore, we next examined the genomic distribution of these
125 markers by chromatin profiling.

126 **MacroH2A1 and H3K27me3 bind broad regions of the host genome that increase during**
127 **infection**

128 We hypothesized that macroH2A1 and H3K27me3 are deposited at specific genomic loci on the
129 host genome during infection to promote the formation of heterochromatin. To test this
130 hypothesis, we used CUT&Tag[20] to profile the genomic localization of macroH2A1 at 4, 8 and
131 12 hours post infection (hpi) in wild-type (WT) and macroH2A1 KO HFF-T cells. We also
132 examined the chromatin profile of H3K27me3 under these conditions. On the human genome,
133 we observed clear enrichment of macroH2A1 and H3K27me3 compared to IgG in WT cells (Fig
134 2a and S1a-b). The enrichment of macroH2A1 and H3K27me3 was observed as large domains
135 that were gained upon viral infection (Fig 2a), suggesting that the host landscape is altered
136 upon infection. These gains were reflected in an increase in total protein levels measured by
137 western blot (Fig 2b). Since large regions are not amenable to traditional peak-based analysis,
138 we instead used domain-based analysis. With the minimum domain size of 1 kb, we observed
139 ~50,000 H3K27me3 domains and ~70,000 macroH2A1 domains genome wide. We observed

140 less than 10 macroH2A1 domains in the datasets generated from macroH2A1 KO cells,
141 indicating that our algorithm was identifying robust domains (Fig S2a). We then calculated the
142 change in enrichments of macroH2A1 domains and used k-means clustering during the time
143 course of infection compared to mock to identify patterns of macroH2A1 gain or loss during
144 infection (Fig 2c and S2b). With k=6, we observed two clusters to substantially gain macroH2A1
145 over the course of infection (Clusters 5 and 6, Fig 2c left and S2d). Clusters 1-3 had significant
146 decreases in macroH2A1, whereas cluster 4 had a minor increase (Fig 2c left, Figure S2d). We
147 then asked how these macroH2A1-defined clusters behaved with respect to H3K27me3 and
148 found that the overall trends across clusters were preserved in H3K27me3 (Fig 2c right and
149 S2e), suggesting that H3K27me3 is largely enriched in the same broad regions. In contrast, the
150 macroH2A1 CUT&Tag on the viral genome showed similar enrichments in both WT and
151 macroH2A1 KO cells. Further, the H3K27me3 signal on the viral genomes also mirrored IgG
152 control. These results indicated that there was a significant background signal from the viral
153 genome that could not be accounted for (Fig S1c-d). Therefore, we disregarded viral genome
154 reads in our dataset. Taken together, these results indicate that multiple forms of
155 heterochromatin were gained at specific host genomic loci during HSV-1 infection.

156 To determine whether H3K27me3 deposition was dependent on macroH2A1, we also examined
157 H3K27me3 domains in the absence of macroH2A1. We plotted the H3K27me3 changes at the
158 same clusters for macroH2A1 KO cells and found that the trends of H3K27me3 were similar
159 between WT and macroH2A1 cells (Fig S2b, c and f). This result suggests that H3K27me3
160 deposition is independent of macroH2A1. In summary, HSV-1 infection results in formation of
161 new heterochromatin domains that span ~10-100s of kilobases. Importantly, our results
162 demonstrate that heterochromatin accumulating in the nuclear periphery during HSV-1 infection
163 represents *new* regions of heterochromatin that are macroH2A1 and H3K27me3 dependent.

164 **MacroH2A1 and H3K27me3 deposition correlates with decreased transcription in active**
165 **compartments**

166 To examine the transcriptional output of newly formed macroH2A1 and H3K27me3-bound
167 regions, we performed RNA-seq on WT and macroH2A1 KO cells over the course of HSV-1
168 infection and calculated fold changes in RNA levels at each time point over the mock control.
169 We identified genes that are contained within domains in each cluster defined in Figure 2 and
170 plotted the distribution of RNA fold changes of the genes grouped by the clusters to which they
171 belonged (Fig S3a). We found that total RNA levels anti-correlate with macroH2A1 presence:

172 clusters 1-3 had an increase in RNA levels, whereas clusters 4-6 had a decrease in RNA levels
173 over the course of infection (Fig S3a). Strikingly, the gene expression changes in macroH2A1
174 KO cells mirror that of WT cells, leading us to conclude that macroH2A1 deposition is not driving
175 changes in total RNA (Fig S3b). To determine whether these changes in RNA reflected changes
176 in transcription, we analyzed published 4sU-RNA-labeling data during HSV-1 infection[21]. We
177 found that overall clusters 4-6 had increased signals compared to clusters 1-3, suggesting that
178 active transcription is occurring in clusters 4-6. Importantly, the time course comparison
179 revealed that in clusters 5 and 6, where we found an increase in macroH2A1 and H3K27me3
180 presence during infection, the 4sU-labeled RNA decreased at 8hpi compared to 4 hpi, indicating
181 that the new heterochromatin is deposited in regions with active transcription (Fig S3c).
182 Interestingly, cluster 4 diverged between total RNA and 4sU-RNA data: 4sU-RNA increased
183 whereas total RNA decreased. This indication of active transcription explains why cluster 4
184 features a weak macroH2A1 gain. Taken together, these results indicate that macroH2A1 and
185 H3K27me3 presence correlates with a decrease in transcription in active regions.

186 Next, we asked if the gain or loss of macroH2A1 happened across previously defined genome
187 compartments[22]. We determined the distribution of the eigenvector corresponding to A/B
188 compartments for IMR90 Hi-C data from the 4DN project[23]. Here, positive values correspond to
189 the A compartment, which features higher gene density and accessible or active chromatin,
190 whereas negative values correspond to the B compartment, which features inactive chromatin.
191 All clusters except cluster 2 are significantly biased towards one of the compartments: clusters 1
192 and 3 are significantly biased towards compartment B, whereas clusters 4-6 are significantly
193 biased towards compartment A (Fig S3d). Strikingly, the median of the clusters increases
194 moving from Cluster 1 to Cluster 6, correlating with macroH2A1 gain. Thus, macroH2A1 gains
195 and losses happen in distinct genomic compartments upon HSV-1 infection. In summary,
196 macroH2A1 and H3K27me3 presence correlates with decreased transcription over the course
197 of HSV-1 infection in active compartments.

198 Because macroH2A1 and H3K27me3-bound regions span a large portion of the host genome,
199 we asked whether any specific gene ontology (GO) categories were over-represented for the
200 genes in each macroH2A1-defined cluster (Fig S4). Genes in clusters 1 and 2 (with decreased
201 macroH2A1 and increased expression) were associated with response to dsRNA and
202 inflammatory responses, as expected during viral infection. Surprisingly, clusters 4-6, with
203 increasing macroH2A1, consisted mostly of housekeeping genes. This suggests that the
204 deposition of macroH2A1 is not directly affecting the expression of specific genes that would be

205 pro- or anti-viral, but rather it is likely that these changes in transcription are a result of the
206 stress response to infection. Furthermore, we quantified total viral RNA via RNA-seq and
207 determined that there were no significant changes in viral RNA accumulation between WT and
208 macroH2A1 KO cells (Fig S3e), suggesting that viral transcription is not affected by the loss of
209 macroH2A1. Therefore, given that heterochromatin in the nuclear periphery surrounds capsids
210 that access the inner nuclear membrane (Fig 1), we considered the scenario in which the
211 chromatin structure generated by newly formed macroH2A1 and H3K27me3 bound regions of
212 the genome was important for viral egress. Therefore, we next examined infection progression
213 in the absence of these markers.

214 **Loss of macroH2A1 or H3K27me3 results in reduced viral progeny but does not affect**
215 **viral genome or protein accumulation**

216 To determine the impact of macroH2A1 in HSV-1 infection, we infected WT and macroH2A1 KO
217 HFF-T cells with HSV-1. Upon infection, we examined viral protein accumulation and observed
218 similar levels of ICP0 (immediate early [24]), VP16 (early [25]) and glycoprotein H (gH, late [26]) in
219 both wild type (WT) and macroH2A1 KO cells (Fig S5a). We next examined HSV-1 replication
220 and measured viral genome accumulation by droplet digital PCR (ddPCR). We observed no
221 significant difference in viral genome accumulation between WT and macroH2A1 KO cells (Fig
222 3a, black and green bars), indicating that neither HSV-1 replication nor protein production is
223 affected by macroH2A1 loss. These results are consistent with no significant changes to viral
224 RNA as measured by RNA-seq (Fig S3e). To determine the impact of macroH2A1 loss on viral
225 progeny production, we measured viral genome accumulation in the supernatant. We
226 discovered a 9-fold decrease in the levels of HSV-1 genomes produced in the supernatant of
227 macroH2A1 KO cells compared to those produced from WT cells at 12 hpi (Fig 3b, green and
228 black bars). We further discovered that infectious progeny produced from macroH2A1 KO cells
229 were significantly decreased compared to those produced from WT cells at 8 and 12 hpi (Fig 3c,
230 green and black bars). This effect was consistent across cell types with similar results observed
231 in macroH2A1 KO RPE cells (Fig S5b-c). Taken together, these data indicate that loss of
232 macroH2A1 leads to a significant defect in productive viral progeny but not viral protein, RNA, or
233 genome accumulation. Therefore, we conclude that macroH2A1 is important for HSV-1 egress.

234 We next examined the impact of H3K27me3 on HSV-1 infection by treatment with tazemetostat
235 to inhibit EZH2 and deplete H3K27me3 levels (as in Fig 1). We treated both WT and
236 macroH2A1 KO cells to examine any synergistic effects of both heterochromatin markers. We

237 found that accumulation of viral proteins ICP0, VP16 and gH were not affected by the reduction
238 of H3K27me3, with or without macroH2A1 (Fig S5d-e). We next examined viral genome
239 accumulation and found that reduction of H3K27me3 did not significantly affect viral genome
240 accumulation compared to control (Fig 3a, black and blue bars). We observed no additional
241 decrease in viral genomes in macroH2A1 KO cells treated with the inhibitor, suggesting that
242 regardless of H3K27me3 levels, loss of macroH2A1 does not impact viral replication as we
243 observed above (Fig 3a, striped bars). We next measured viral genomes in the supernatant to
244 determine the impact of H3K27me3 reduction on progeny production and found a significant 4-
245 fold decrease at 12 hpi from inhibitor-treated cells compared to DMSO-treated (Fig 3b, blue
246 bars). Further, we found infectious progeny produced from inhibitor-treated cells were reduced
247 significantly at 12 hpi compared to those produced from control cells (Fig 3c, blue bars).
248 Interestingly, H3K27me3 reduction in macroH2A1 KO cells does not result in any additional
249 defects, suggesting the two markers function in the same genetic pathway (Fig 3a-c, striped
250 bars). These results are consistent with a previous report that found HSV-1 titers, but not viral
251 replication, were reduced upon EZH2 inhibition[27]. Furthermore, we did not observe any
252 significant differences in the ratio of genomes to plaque forming units (pfu) upon loss of
253 macroH2A1, H3K27me3, or both, compared to control conditions (Fig S5f), indicating that loss
254 of these markers does not result in significantly more defective particles. Taken together, these
255 results indicate that H3K27me3 and macroH2A1 are important for efficient viral egress.

256 To determine how robust the requirement for macroH2A1-dependent chromatin is for HSV-1
257 egress, we used clinical HSV-1 viruses isolated from “low-shedding” or “high-shedding” patients.
258 We measured protein accumulation at 4, 8, and 12 hpi and viral genome accumulation in cells
259 and supernatant by ddPCR. We found that there was no significant change in viral protein or
260 viral genome accumulation for either clinical isolate in macroH2A1 KO cells (Fig 3d and S5g-h).
261 We measured viral genomes in the supernatant and found that there was a modest reduction in
262 HSV-1 genomes in the supernatant of macroH2A1 KO cells compared to control cells (Fig 3e,
263 green bars). For both clinical isolates, we found that macroH2A1 KO cells produced significantly
264 fewer progeny than WT cells at 12 hpi (Fig 3f). Taken together, these results indicate that
265 egress of clinically isolated HSV-1 is also dependent on macroH2A1.

266

267 **MacroH2A1 or H3K27me3-dependent heterochromatin in the nuclear periphery is critical**
268 **for efficient HSV-1 nuclear egress**

269 Our results indicate that HSV-1 capsids in the nucleus access the nuclear membrane through
270 channels bracketed by highly dense chromatin at the nuclear periphery (Fig 1), consistent with
271 previous reports in other cell types[8,16]. We found that loss of macroH2A1 or depletion of
272 H3K27me3 resulted in decreased heterochromatin in the nuclear periphery (Fig 1) and caused a
273 decrease in productive viral progeny (Fig 3). Therefore, we hypothesized that efficient HSV-1
274 egress out of the nuclear compartment requires macroH2A1- or H3K27me3-dependent
275 heterochromatin in the nuclear periphery. To test this, we infected macroH2A1 KO cells,
276 visualized nuclei by TEM and quantified capsids in the nucleus (Fig 4a). We found that infected
277 macroH2A1 KO nuclei have significantly more HSV-1 capsids than those of WT cells (Fig 4a),
278 indicating that loss of macroH2A1-dependent heterochromatin is detrimental for efficient nuclear
279 egress. Similarly, we used tazemetostat treatment to deplete H3K27me3 levels, infected cells
280 with HSV-1, and visualized capsids in the nuclei of infected cells by TEM. Strikingly, we found
281 that significantly more capsids accumulated at the nuclear membrane compared to control cells
282 (Fig 4b). We quantified this difference by scoring whether more than three capsids interacted
283 with the inner nuclear membrane at any one location. Taken together, these results indicate that
284 both macroH2A1 and H3K27me3-dependent heterochromatin in the nuclear periphery are
285 crucial for successful viral nuclear egress.

286 To determine whether capsid assembly was impacted by heterochromatin disruption, we
287 quantified capsid type as a proportion of the total capsids from our TEM. Herpesvirus infection
288 produces three subtypes of capsids: A capsids are empty, B capsids contain scaffolding
289 proteins, and C capsids contain viral gDNA and are considered the precursor to infectious
290 virions[28,29] (Fig S6a). We quantified the proportion of each capsid type in WT and macroH2A1
291 KO cells and found no difference in the proportion of each capsid type (Fig S6b-c). We carried
292 out the same analysis upon infection in H3K27me3-depleted cells and similarly found no
293 difference in the proportion of capsid type (Fig S6c). In summary, these results indicate that
294 capsid formation is not impacted by disruption of heterochromatin. Rather, the ability of the
295 capsids to egress from the nuclear compartment is dependent on heterochromatin formation.
296 Taken together, these data demonstrate that macroH2A1 and H3K27me3-dependent
297 heterochromatin in the nuclear periphery is critical for efficient nuclear egress.

298

299 **DISCUSSION**

300 Host chromatin is emerging as a critical barrier to viral success. Elegant electron microscopy
301 work showed that HSV-1 infection induces host chromatin redistribution to the nuclear
302 periphery[2,8]. Here, we showed that viral capsids subsequently egress through regions of less
303 dense staining or heterochromatin channels (Fig 1), consistent with reports in different cell
304 types[16]. We investigated the impact of heterochromatin markers histone variant macroH2A1 and
305 H3K27me3 on chromatin architecture and HSV-1 infection. We found that loss of macroH2A1
306 resulted in significantly less heterochromatin visible in the nuclear periphery by TEM in HFF
307 cells (Fig 1), similar to what was observed in hepatoma cells[13]. To our knowledge, this is the first
308 instance of TEM imaging of heterochromatin upon depletion of H3K27me3, which produced a
309 similar phenotype to macroH2A1 KO with significantly less heterochromatin in the nuclear
310 periphery (Fig 1). We then demonstrated that macroH2A1 and H3K27me3 bind broad regions of
311 the host genome that increase during HSV-1 infection (Fig 2). Our chromatin profiling analysis
312 required a custom algorithm to accommodate the massive domains created by macroH2A1 and
313 H3K27me3, consistent with regions large enough to be visible by TEM. We demonstrated that
314 these regions are primarily found in transcriptionally active compartments defined by Hi-C,
315 supporting the idea that newly formed heterochromatin increases during HSV-1 infection. We
316 further showed that loss of macroH2A1 or depletion of H3K27me3 did not impact viral
317 replication or protein production but resulted in significantly reduced infectious progeny (Fig 3).
318 Finally, we demonstrated by TEM that in the absence of macroH2A1, significantly more viral
319 capsids were trapped in the nucleus (Fig 4). Interestingly, the phenotype by TEM of H3K27me3
320 depletion on HSV-1 capsid accumulation was more striking with capsids lined up at the inner
321 nuclear membrane (Fig 4). We found significantly more instances of greater than 3 capsids
322 interacting with the nuclear membrane than in control cells, suggesting that capsids were unable
323 to egress without H3K27me3-dependent heterochromatin. Together, these results support a
324 model in which host heterochromatin formation acts as a structural highway for HSV-1 capsids
325 to successfully access the inner nuclear membrane (Fig 4c).

326 Mining of proteomics on histone marks indicates that several heterochromatin marks including
327 H3K9me3 are also changing during HSV-1 infection[3]. This suggests that there may be other
328 mechanisms of heterochromatin dynamics at play. It will be fascinating to consider the diverse
329 implications of heterochromatin domains not only as a means of transcriptional regulation but
330 also as a structural component that impacts many facets of viral infection. Interestingly, a recent
331 study examined chromatin accessibility changes upon HSV-1 infection compared to heat shock

332 or salt stress and found that changes to chromatin were similar amongst these different
333 conditions[30]. Together with our findings, this suggests that the global changes to
334 heterochromatin are likely a consequence of the cell's stress response to infection that HSV-1
335 exploits to access the inner nuclear membrane. Our results strongly indicate that it is the
336 structural aspect of peripheral heterochromatin that is important for nuclear HSV-1 egress rather
337 than transcription of any single gene or group of genes. Therefore, we propose that deposition
338 of macroH2A1 and H3K27me3 in specific genomic regions during HSV-1 infection supports the
339 formation of heterochromatin channels through which HSV-1 capsids travel to reach the inner
340 nuclear membrane. At the inner nuclear membrane, capsids are aided by the nuclear egress
341 complex, comprised of viral proteins UL34 and UL31, to bud into the inner nuclear membrane
342 and fuse with the outer nuclear membrane for further maturation in the cytoplasm[7]. Budding into
343 the nuclear membrane also requires nuclear lamina disruption. Multiple reports describe that not
344 only does lamina disruption occur independently of capsid formation, but that chromatin is likely
345 the limiting factor in viral egress[31–36]. Together with our results, this suggests that there are
346 multiple steps in the capsid's journey to the inner nuclear membrane preceding nuclear budding.
347 In summary, our study demonstrates that the contribution of heterochromatin to the successful
348 egress of HSV-1 capsids is a critical aspect of viral infection.

349

350 **AUTHOR CONTRIBUTIONS**

351 Conceptualization, H.C.L, L.K.M., and D.C.A; methodology H.C.L, L.K.M., and D.C.A.; formal
352 analysis, H.C.L, L.K.M., S.R., and D.C.A.; investigation, H.C.L, L.K.M., M.R.B., H.E.A, E.E.A,
353 and D.C.A; resources, H.C.L, L.K.M., M.R.B., H.E.A, E.E.A, S.R., and D.C.A.; data curation,
354 H.C.L, L.K.M., M.R.B., S.R., and D.C.A.; writing – original draft, H.C.L, L.K.M., M.R.B., S.R., and
355 D.C.A.; writing – review & editing, H.C.L, L.K.M., M.R.B., H.E.A, E.E.A, S.R., and D.C.A.;
356 visualization, H.C.L, L.K.M., S.R., and D.C.A.; supervision, H.C.L, L.K.M., and D.C.A.; funding
357 acquisition, H.C.L., E.A.A, S.R., and D.C.A.

358

359 **ACKNOWLEDGEMENTS**

360 We thank members of the Avgousti lab, M. Emerman, A. Geballe, M. Lagunoff, K. Lynch, S.
361 Parkhurst, and M. Weitzman for insightful comments. We thank D. Janssens and the Henikoff
362 lab for reagents and assistance with CUT&Tag. We thank the Salama and Overbaugh labs for
363 assistance with ddPCR. We thank the Jerome lab for the clinical HSV isolates and the Cellular

364 Imaging, Electron Microscopy (EMSR), F. Wu and Genomics & Bioinformatics Shared Resource
365 Facilities at the Fred Hutchinson Cancer Research Center for help with sequencing and data
366 analysis. We thank J. Dubrulle and the Cellular Imaging Shared Resource (CISR) for help with
367 image analysis. The EMSR, CISR, and Genomics core are supported in part by the Fred
368 Hutch/University of Washington Cancer Consortium (P30 CA015704). This study was supported
369 by start-up funds from the RNA Bioscience Initiative at the University of Colorado School of
370 Medicine (S. R.), the Fred Hutch (D.C.A.), and NIH funding to H.C.L. (AI083203), E.A.A.
371 (AI083203), S.R. (GM133434), and D.C.A. (GM133441).

372

373

374 **FIGURES**

Figure 1. HSV-1 capsids traverse channels of less dense chromatin to reach the inner nuclear membrane.

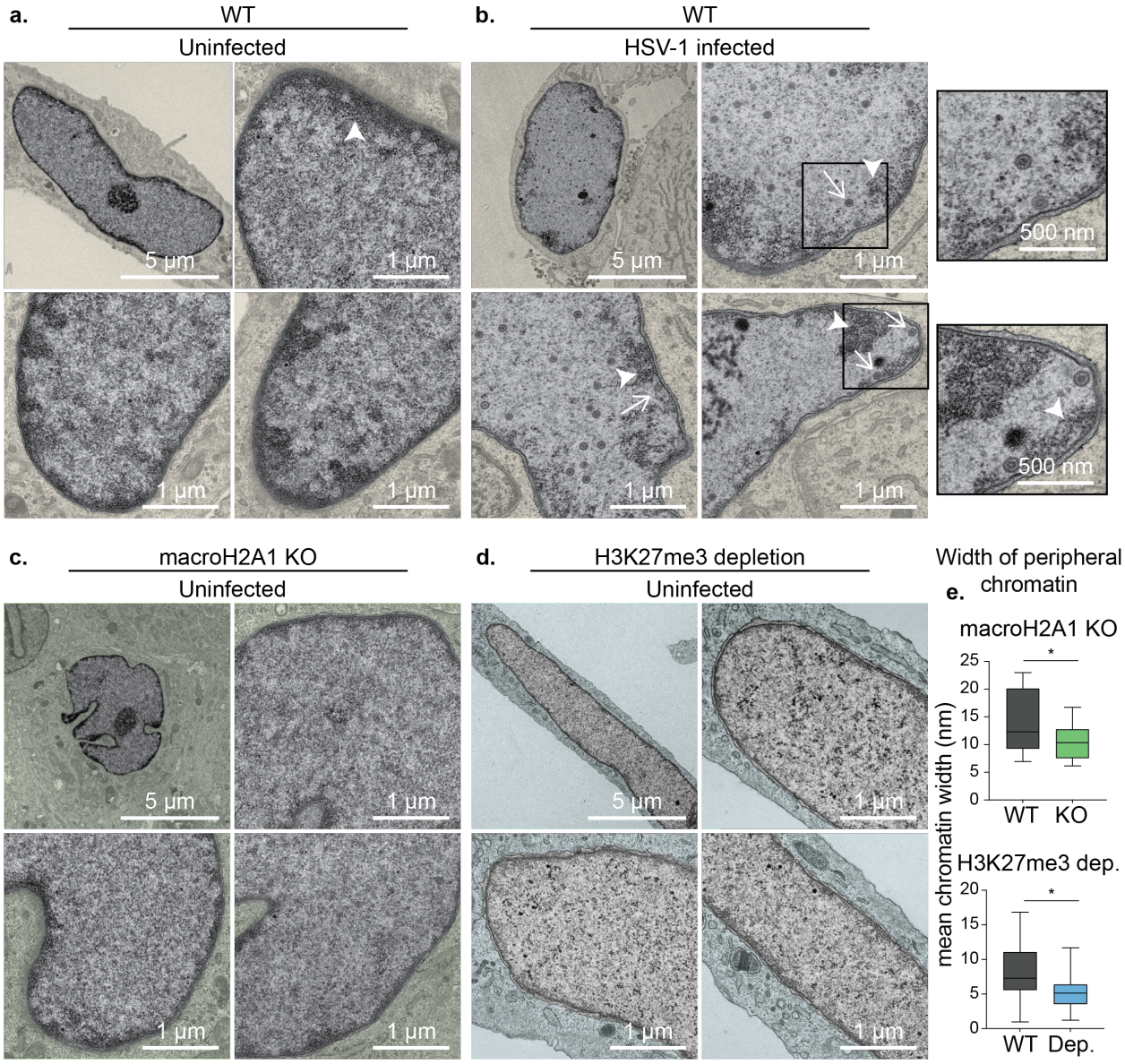

375

376

377 **Figure 1. HSV-1 capsids traverse channels of less dense chromatin to reach the inner**

378 **nuclear membrane.**

379 a) Transmission electron microscopy (TEM) images of representative uninfected nuclei in

380 WT HFF-Ts. Regions outside of the nucleus are colorized yellow. Dark regions represent

381 high density heterochromatin (arrowhead). Scale bar as indicated.

382 b) TEM images of representative WT nuclei at 18 hours post-infection with HSV-1. Insets
383 show enlarged views of respective boxed areas containing heterochromatin channels
384 within nuclei. Arrowhead indicates heterochromatin, arrows indicate HSV-1 capsids.
385 Scale bar as indicated.
386 c) TEM images of representative uninfected nuclei in macroH2A1 knockout HFF-Ts.
387 Regions outside of the nucleus are colorized green. Scale bar as indicated.
388 d) TEM images of representative uninfected nuclei in H3K27me3 depleted HFF-Ts.
389 Regions outside of the nucleus are colorized blue. Scale bar as indicated.
390 e) (Top) Quantification of peripheral heterochromatin width in nuclei from A and C. Width
391 was measured in nm from the nuclear periphery via binary thresholding from intensity
392 profiles sampled every 10 pixels. Mean width was plotted for each nucleus. $p= 0.0275$
393 ($n=16$ WT, $n=22$ macroH2A1 KO). (Bottom) Quantification as above in nuclei from A and
394 D ($p= 0.0144$, $n= 22$ WT, $n=20$ H3K27me3 depleted).
395
396
397
398
399
400

Figure 2. MacroH2A1 and H3K27me3 bind broad chromatin regions on the host genome.

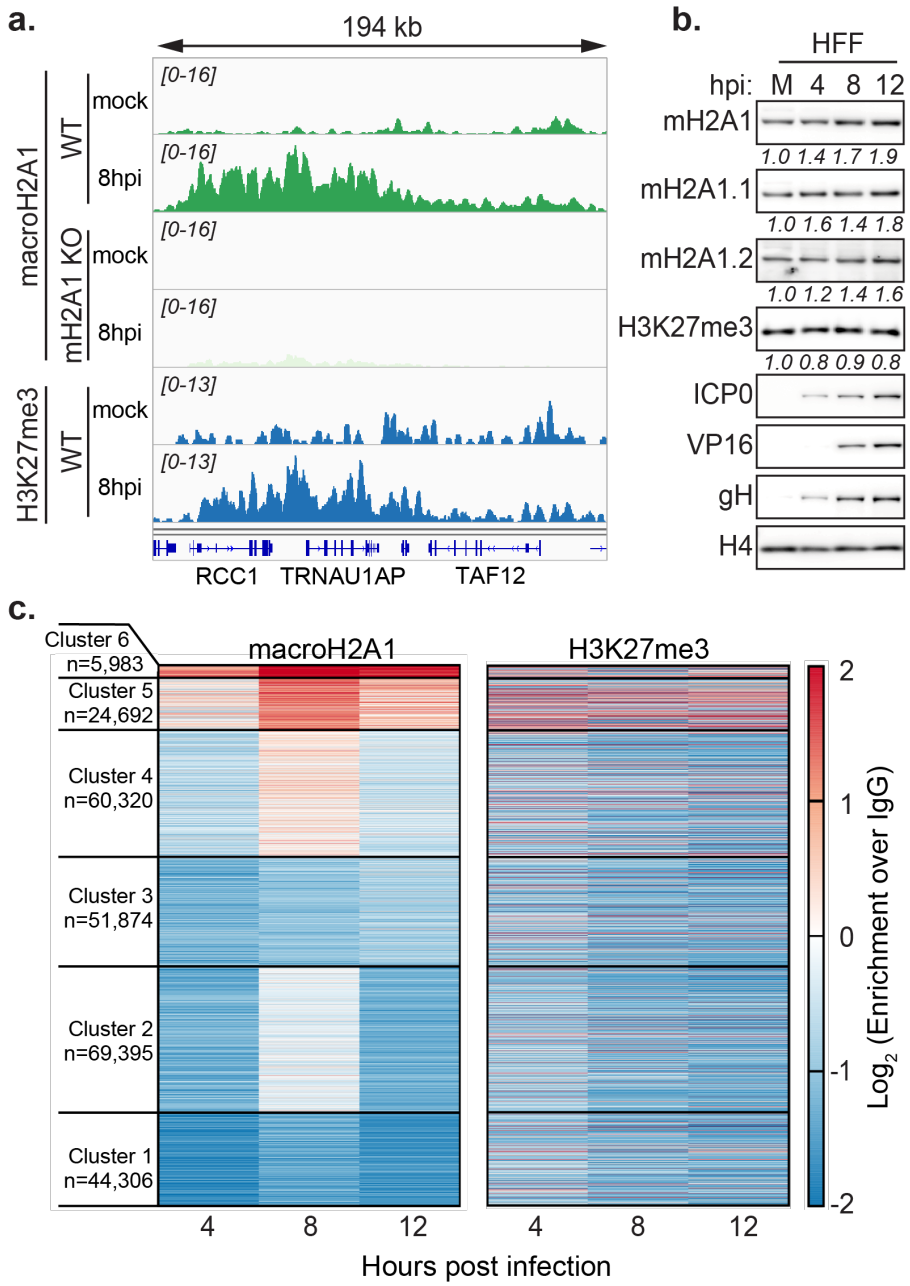

Figure 2. MacroH2A1 and H3K27me3 bind broad chromatin regions on the host genome.

a) Representative genome browser snapshots of spike-in normalized CUT&Tag enrichment of macroH2A1 and H3K27me3 showing increases at 8hpi of HSV-1 infection as measured by CUT&Tag in WT or macroH2A1 KO as indicated. The region shown is found on chromosome 1.

408 b) Western blot of total macroH2A1, macroH2A1.1, macroH2A1.2 isoforms, and
409 H3K27me3 during mock (M) or HSV-1 infection 4-, 8-, and 12-hpi. ICP0, VP16, gH are
410 viral proteins, H4 is shown as a loading control. Quantification of relative intensity of H4
411 normalized to the mock samples are shown.
412 c) Changes in log2 enrichment of spike-in normalized CUT&Tag of macroH2A1 and
413 H3K27me3 over IgG compared to mock treatment are shown as a heatmap. Each line in
414 the heatmap represents a domain of macroH2A1.

415
416
417

Figure 3. HSV-1 requires heterochromatin marks macroH2A1 and H3K27me3 for progeny production but not replication.

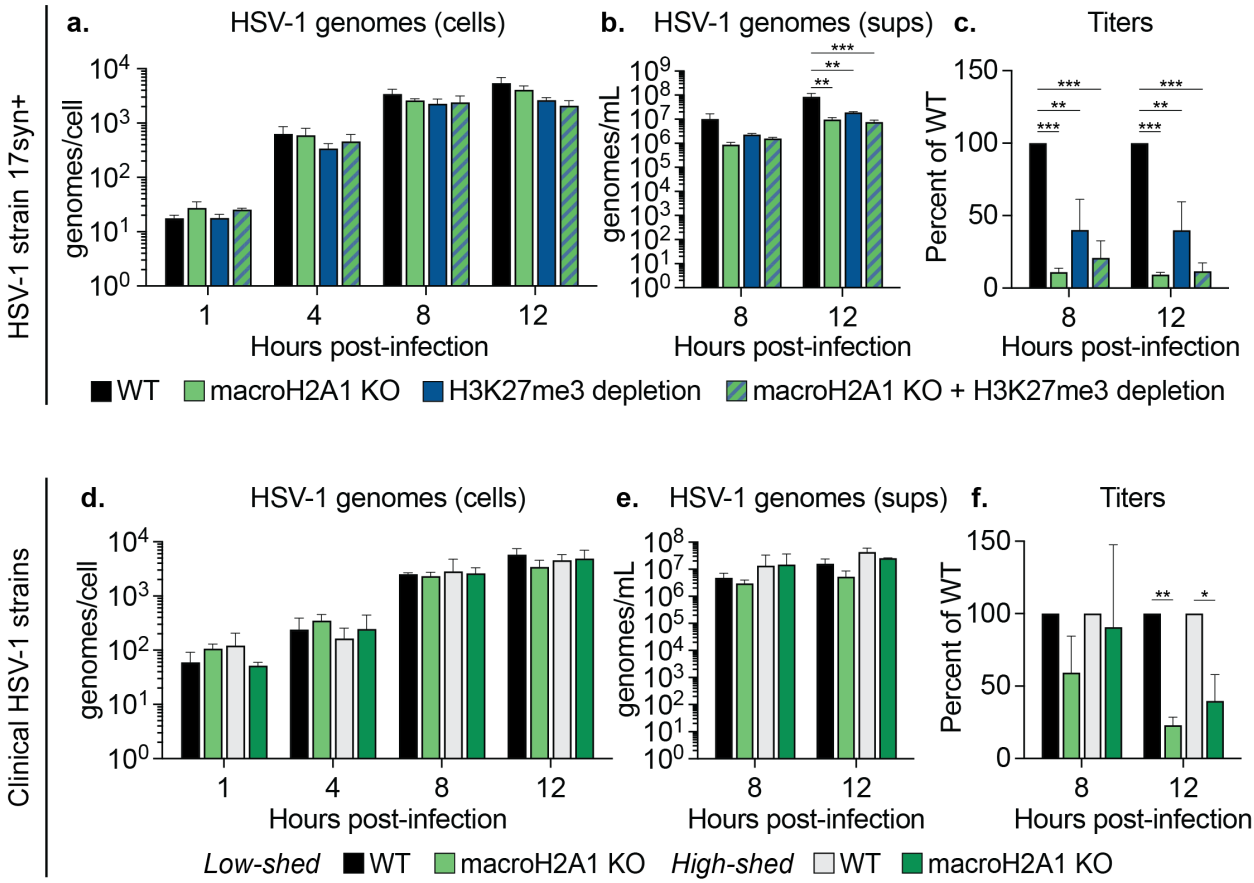

418
419
420

421 **Figure 3. HSV-1 requires heterochromatin marks macroH2A1 and H3K27me3 for progeny**
422 **production but not replication.**

423 a) Droplet digital (ddPCR) quantification of HSV-1 genomes extracted from infected cells as
424 indicated for each time point. Error bars represent the SEM of three biological replicates.
425 b) ddPCR quantification of HSV-1 genomes released from cells treated as indicated and
426 isolated from supernatants (sups). Error bars represent the SEM of three biological
427 replicates, ** $p < 0.01$, *** $p < 0.001$.
428 c) Infectious progeny produced from HSV-1 infected cells treated as indicated and
429 quantified by plaque assay. Viral yield is indicated as the percent yield compared to WT
430 and was calculated through dividing plaque-forming units (pfu) per mL of the treatment
431 group titers by the WT titers of each respective virus at each indicated time point. ** $p <$
432 0.01, *** $p < 0.001$.
433 d) ddPCR quantification as in (a) from infection with low- and high-shedding clinical isolates
434 of HSV-1. Error bars represent the SEM of three biological replicates.
435 e) ddPCR quantification as in (b) of HSV-1 genomes from cells infected with clinical
436 isolates of HSV-1 as indicated. Error bars represent the SEM of three biological
437 replicates.
438 f) Infectious progeny of cells as indicated infected with clinical HSV-1 isolates quantified by
439 plaque assay. Viral yield is indicated as the percent yield compared to WT, * $p. < 0.05$, **
440 $p < 0.01$.

441

442

Figure 4. HSV-1 requires macroH2A1- and H3K27me3-dependent heterochromatin for efficient egress.

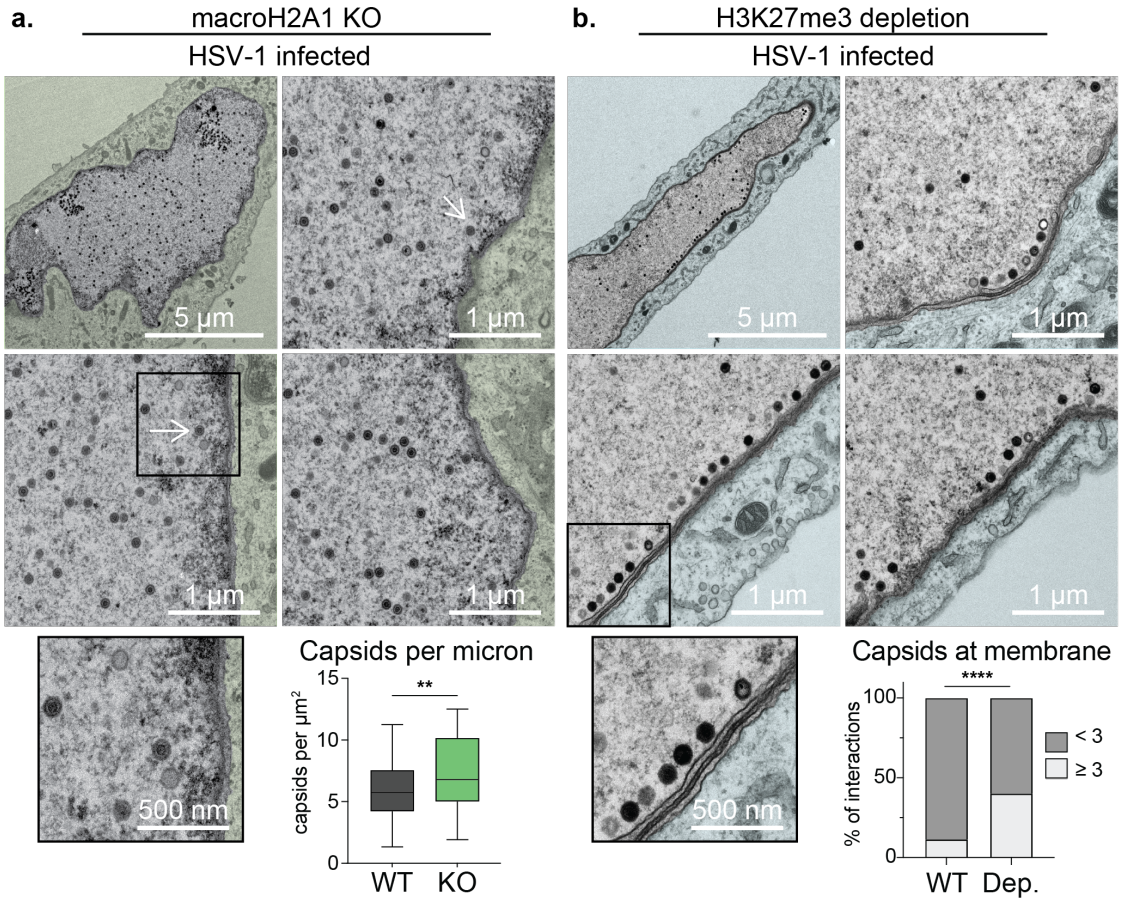

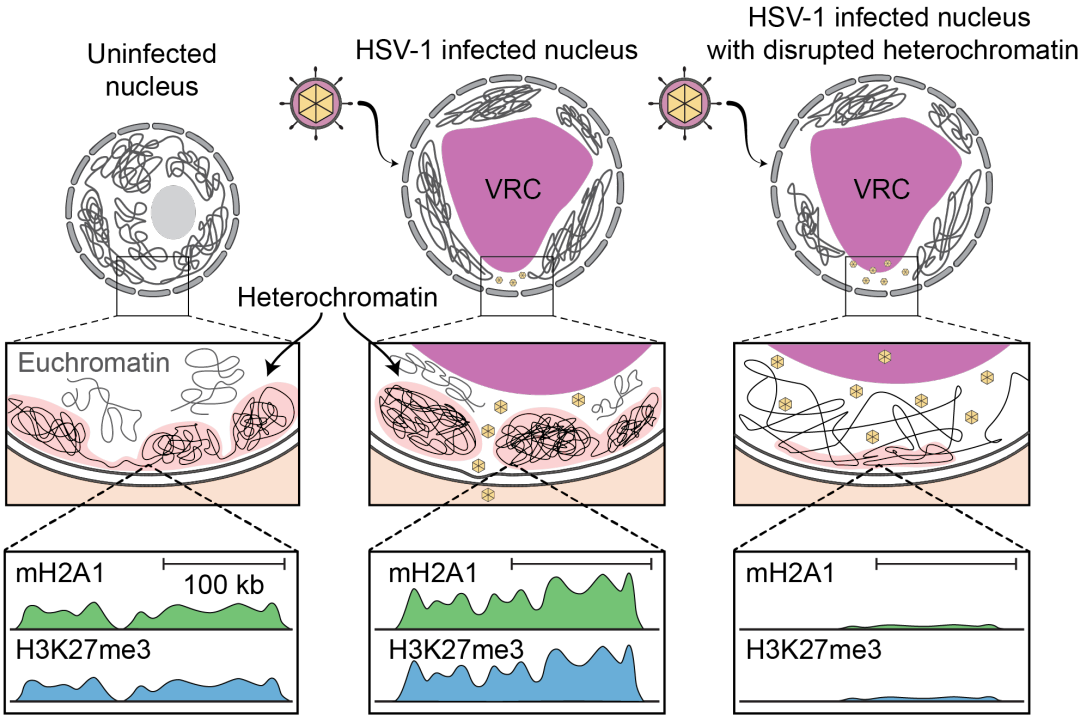

443

444 **Figure 4. HSV-1 requires macroH2A1- and H3K27me3-dependent heterochromatin for**
445 **efficient egress.**

446 a) TEM images of representative macroH2A1 KO nuclei infected with HSV-1. Insets show
447 enlarged views of respective boxes. Arrows indicate HSV-1 capsids. Scale bar as
448 indicated. (Bottom Right) Quantification of capsids within nuclei compared to Figure 1b.
449 Number of capsids was normalized according to nucleus area in mm^2, p=0.0036 (n=40
450 WT, n=55 mH2A1 KO).

451 b) TEM images of representative H3K27me3 depleted nuclei infected with HSV-1
452 presented as in (a). (Bottom Right) Quantification of the number of capsids at the
453 nuclear periphery compared to Figure 1b, p=0.0001 (n=8 cells for DMSO, n=5 cells for
454 H3K27me3 depleted).

455 c) Model for heterochromatin support of HSV-1 egress. In uninfected cells (left),
456 heterochromatin is enriched in the nuclear periphery. Upon infection with HSV-1
457 (middle), there is an increase in heterochromatin at specific regions in the nuclear
458 periphery that results in formation of heterochromatin channels that allow capsids to
459 traverse from the viral replication centers (VRCs) to the inner nuclear membrane where
460 they bud into the perinuclear space and subsequently fuse with the outer nuclear
461 membrane into the cytoplasm. In infected cells missing heterochromatin markers
462 macroH2A1 or H3K27me3 (right), these heterochromatin channels cannot form properly
463 which results in increased capsids trapped in the nuclear compartment.

464

465

466

467 **MATERIALS AND METHODS**

468 **Cells and viruses:**

469 Primary human foreskin fibroblasts (HFFs), hTERT-immortalized HFFs, and hTERT-
470 immortalized macroH2A1 knockout HFFs were cultured using standard methods with 10% FBS
471 and 1% penicillin-streptomycin as previously described[37]. Cells were grown at 37 °C with 5%
472 CO_2 and tested for mycoplasma contamination approximately once a month.

473 The lab adapted strain of HSV-1, *syn 17+* [38] was used for all experiments unless otherwise
474 noted. Monolayers of cells were infected for 1 hour at 37 °C as previously described [39]. An MOI
475 of 3 was used for all experiments, except for EM samples which used MOI of 10. Cells were
476 collected at mock, 4-, 8-, and 12- hpi for western blot. Supernatant was collected at 8- and 12-
477 hpi for plaque assays. Virus stock was grown by infecting Vero cells at an MOI of 0.0001. Virus
478 was harvested ~60-80 hours post-infection and titered on U2OS cells to determine stock plaque
479 forming units per mL (PFU/mL). Experimental plaque assays were set up in Vero cells. Plaque
480 assays were set up on serial 10-fold dilutions in serum-free DMEM. Virus was left on cells for 1
481 hour then aspirated. Cells were washed with 1X PBS (pH 7.46) and 2% methylcellulose overlay
482 in DMEM with 2% FBS and 0.5% penicillin-streptomycin was added to wells. Plaques were fixed
483 with 0.2% crystal violet between 96-100 hours post infection and plaques were counted by
484 hand. All plaque assays were set up with 2 technical replicates.

485 Clinical isolates were acquired in 1994 and 1995 from oral swab collections. Samples were de-
486 identified on collection. Patients provided daily home collections of oral swabs, and qPCR was
487 used to detect how many days HSV was detected in these swabs. Patients that had detectable
488 HSV in only a few swabs were classified as “low-shedders” and patients that had a high
489 percentage of days with positive swabs were classified as “high-shedders.” Stocks were a gift
490 from the lab of Keith Jerome.

491 Table 1: Cell line sources.

Cell Line	Source
Human: RPE-1 (hTERT-immortalized)	Gift of E. Hatch Lab [40] (Invitrogen)
Human: Primary HFF	Gift of D. Galloway Lab
Human: HFF (hTERT-immortalized)	Gift of J. Kamil Lab [41]
African Green Monkey: Vero	Gift of A. Geballe Lab [42]

492

493

494 **Knockout of macroH2A1:**

495 MacroH2A1 guide RNA (gRNA, see Table 3) was cloned into TLCv2 (Addgene plasmid: 87360),
496 a plasmid encoding doxycycline-inducible Cas9-2A-GFP and gRNA expression. To generate
497 lentiviral particles, $1.0x10^7$ HEK293T cells were transfected with 12 µg TLCV2_sg_mH2A1, 8 µg
498 pMDL (Addgene plasmid: 12251), 4 µg VSVg, and 2.5 µg pREV (Addgene plasmid: 115989)
499 using Attractene transfection reagent (Qiagen: 301005). Lentivirus was harvested at 24-, 48-,
500 and 72-hours post-transfection, filtered through 0.2 µm filters, aliquoted, flash frozen with liquid
501 nitrogen, and stored at -80C. 2 mL of thawed filtered lentivirus was used to transduce
502 approximately $2.25x10^6$ HFF-T or $3x10^6$ RPE cells in 10 cm plates with 8 µg/mL polybrene
503 (Millipore-Sigma: TR-1003-G). Cells were allowed to reach confluence before selection with 1
504 µg/mL puromycin for 3 days. Cells were then sorted by GFP positivity or counted by
505 hemocytometer, plated at 1 cell per well into 96-well plates, and selected through serial
506 expansion of colonies. Selected cells were screened for macroH2A1 knockout by western blot.

507 **Infections with tazemetostat pretreatment:**

508 HFFs and macroH2A1 KO HFFs were treated with DMSO or 10 µM of tazemetostat (MedChem:
509 HY-13803) in DMSO for 3 days prior to infection. Cells were then infected at MOI of 3 and after
510 1 hour of incubation with virus, fresh media with 10µM Taz was added to previously treated
511 cells. Control samples were treated with equivalent volumes of DMSO. Samples were harvested
512 as above.

513 **Western Blotting:**

514 Western blotting was performed as previously described [37]. Briefly, cells were counted, pelleted,
515 resuspended in 1x NuPAGE lithium dodecyl sulfate (LDS) sample buffer (Fisher Scientific:
516 NP007) + 5% 2-betamercaptoethanol, and boiled for 15 minutes. Protein lysates were
517 separated by 13.5% SDS-PAGE gels using NuPAGE MOPS buffer (Fisher Scientific: NP0001)
518 at 75 volts for 30 minutes then 110 volts for 100 minutes, then transferred to a nitrocellulose
519 membrane (Bio-Rad) at 100 volts for 70 minutes using Transfer Buffer (25 mM Tris Base, 100
520 mM glycine, 20% methanol). Membranes were ponceau stained and imaged. Membranes were
521 blocked in 5% milk in Tris-buffered saline with Tween (TBST) for 1 hour, then probed with
522 primary antibody overnight (see Table 2). Membranes were washed with TBST for thirty
523 minutes, incubated with secondary antibodies conjugated to horseradish peroxidase (α-mouse
524 or α-rabbit; 1:5000) at room temperature for 1 hour, washed with TBST for thirty minutes, and
525 detected using Clarity Western ECL Substrate (Bio-Rad: 1705061) and Chemidoc MP Imaging
526 System (Bio-Rad). Images were formatted using Adobe Photoshop and Illustrator.

527 Table 2: Sources and identification of antibodies used.

Antibody	Source	Identifier	Use (Concentration)
Mouse anti-actin	Abcam	Cat: 5441	WB (1:10,000)
Mouse anti-gH	Abcam	Cat: 110227	WB (1:1,000)
Rabbit anti-H3	Abcam	Cat: 1791	WB (1:20,000)
Rabbit anti-H3K27me3	Cell Signal Technologies	Cat: 9733T	WB/CUT&Tag (1:100)
Rabbit anti-H3K9me3	Abcam	Cat: 8898	WB (1:1,000)
Rabbit anti-H4	Abcam	Cat: 10158	WB (1:1,000)
Mouse anti-ICP0	Santa Cruz Biotechnology	Cat: 53070	WB (1:1,000)
Rabbit anti-macroH2A1	Abcam	Cat: 37264	WB (1:1,000) CUT&Tag (1:100)
Rabbit anti-macroH2A1.1	Cell Signaling Technology	Cat: 12455S	WB (1:1,000)
Mouse anti-macroH2A1.2	Cell Signaling Technology	Cat: 4827S	WB (1:1,000)
Rabbit anti-macroH2A2	Active Motif	Cat: 39874	WB (1:1,000)
HRP-conjugated anti-VP16	Santa Cruz Biotechnology	Cat. 7546	WB (1:1,000)
Peroxidase-AffiniPure Goat Anti-Mouse	Jackson Immunoresearch Laboratories	Cat: 115-035-003	WB (1:5,000)
Peroxidase-AffiniPure Goat Anti-Rabbit	Jackson Immunoresearch Laboratories	Cat: 111-035-045	WB (1:5,000)
Rabbit anti-mouse IgG	Abcam	Cat: 46540	CUT&Tag (1:100)
Guinea pig anti-rabbit IgG	Antibodies Online	Cat: AB1N101961	CUT&Tag (1:100)

528

529 **Quantification of HSV-1 genomes by ddPCR:**

530 Cells were harvested at the indicated times post-infection by trypsinization, washed with 1X
531 PBS and centrifuged at 5000 xg for 2 minutes. Pellets were flash-frozen in liquid nitrogen and
532 stored at -80 °C until processed. HSV-1 DNA within cells was isolated from frozen pellets using
533 QIAamp DNAMini Kit (Qiagen: 51304).

534 Supernatants were harvested at the indicated times post-infection, centrifuged at > 3500 xg and
535 filtered through 40 micron sterile syringe filters. DNA on the exterior of filtered capsids was
536 digested for 1 hour at 25 °C with 20.3 units DNase (Qiagen: 79254) supplemented with 10 mM

537 $MgCl_2$. DNase was inactivated at 75 °C for 10 minutes followed by vortexing. Capsids were
538 digested with 3 mg/mL proteinase K (Fisher Scientific: BP1700) in 100 mM KCl, 25 mM EDTA,
539 10 mM Tris-HCl pH 7.4 and 1% Igepal for 1 hour at 50 °C. HSV-1 genomes from digested
540 capsids were isolated using QIAamp DNAMini Kit.

541 A duplexed droplet digital PCR was performed to measure the levels of cellular or supernatant
542 HSV-1 genomes on the QX100 droplet digital PCR system (Bio-Rad Laboratories, Hercules,
543 CA) using a primer/probe set specific to HSV-1 gB. Cell numbers were determined using a
544 primer/probe set specific to human Beta-globin, a reference gene that exists at two copies per
545 cell. See Table 3 for oligonucleotide sequences, as have been previously established for HSV-
546 1[43]. The digital droplet PCR (ddPCR) reaction mixture consisted of 12.5 µL of a 2X ddPCR
547 Supermix for Probes no dUTP (Bio-Rad: 1863024), 1.25 µL of each 20X primer-probe mix, and
548 10 µL of template DNA. 20 µL of each reaction mixture was loaded onto a disposable plastic
549 cartridge (Bio-Rad: 1864008) with 70 µL of droplet generation oil (Bio-Rad: 1863005) and
550 placed in the droplet generator (Bio-Rad). Droplets generated were transferred to a 96-well PCR
551 plate (Bio-Rad 12001925), and PCR amplification was performed on a Bio-Rad C1000 Touch
552 Thermal Cycler with the following conditions: 95 °C for 10 minutes, 40 cycles of 94 °C for 30
553 seconds, and 60 °C for 1 minute, followed by 98 °C for 10 minutes and ending at 4 °C. After
554 amplification, the plate was loaded onto the droplet reader (Bio-Rad: QX200), and the droplets
555 from each well of the plate were automatically read with droplet reader oil (Bio-Rad: 186-3004)
556 at a rate of 32 wells per hour. Data were analyzed with QuantaSoft analysis software and
557 quantitation of target molecules presented as copies per µL of PCR reaction. HSV-1 genome
558 values were standardized to cellular β-globin levels. Experiments were completed in biological
559 triplicate and statistical analysis was performed using Prism v10 (GraphPad Software).

560 Table 3: Primers used for knockout and ddPCR

CRISPR MacroH2A1 gRNA	CCTCAATAGCAAGCCATCCTGT
HSV1_gB_qPCR_F1	CCGTCAGCACCTTCATCGA
HSV1_gB_qPCR_R1	CGCTGGACCTCCGTGTAGTC
HSV1_gB_probe1	6FAM-CCACGAGATCAAGGACAGCGGCC-BHQ1
beta-globin_qPCR_F1	TGAAGGCTCATGGCAAGAAA
beta-globin_qPCR_R1	GCTCACTCAGTGTGGCAAAGG
beta-globin_probe2_hex	/5HEX/TC CAG GTG AGC CAG GCC ATC ACT A/3BHQ_1/

561

562

563 **Cleavage Under Targets & Tagmentation (CUT&Tag):**

564 Two biological replicates per time point were obtained from independent infections. Protocol
565 was adapted from the established CUT&Tag methods[20]. Cells were harvested using trypsin,
566 washed three times with ice-cold phosphate-buffered saline (PBS) via centrifugation at 600 xg
567 for 3 minutes and counted using a hemocytometer. Nuclei from 600,000 cells were isolated by
568 hypotonic lysis in 1 mL buffer NE1 (20 mM HEPES-KOH pH 7.9; 10 mM KCl; 0.5 mM
569 spermidine; 0.1% Triton X-100; 20% Glycerol; Roche EDTA-free protease inhibitor) for 10
570 minutes on ice followed by centrifugation at 1300 xg for 4 minutes. Nuclei were resuspended in
571 Wash buffer (20 mM HEPES-NaOH pH 7.5; 150 mM NaCl; 0.5 mM spermidine; Roche EDTA-
572 free protease inhibitor) and counted using a hemocytometer. BioMag Plus Concanavalin A
573 coated beads (Polysciences: 86057-3) were equilibrated with Binding buffer (20 mM HEPES-
574 KOH pH 7.9; 10 mM KCL; 1mM $CaCl_2$; 1 mM $MnCl_2$). Beads (5 µL) were mixed with aliquots of
575 75,000 nuclei and incubated at 25 °C for 10 minutes followed by magnetic separation of beads.
576 Beads were resuspended in 50 µL primary antibody [anti-mH2A1 (Abcam: ab37624), anti-
577 H3K27me3 (Cell Signaling:9733) or anti-mouse IgG (Abcam: ab46540) in Wash buffer
578 supplemented with 2 mM EDTA and 0.1% bovine serum albumin (BSA) and incubated on a
579 nutator at 4 °C overnight. The beads were decanted on a magnet stand then resuspended in 50
580 µL secondary antibody [Guinea pig anti-rabbit IgG (Antibodies-Online: ABIN101961) 1:100] in
581 Wash buffer supplemented with 2 mM EDTA and 0.1% BSA and incubated on a nutator at room
582 temperature for 1 hour. The beads were decanted on a magnet stand and washed with 200 µL
583 Wash buffer, then were resuspended in 50 µL pA-Tn5 (1:200) in 300-Wash buffer (Wash buffer
584 containing 300 mM NaCl) and incubated on a nutator at room temperature for 1 hour. The
585 beads were washed twice with 200 µL 300-Wash buffer, then resuspended in 50 µL
586 Tagmentation buffer (300-Wash buffer supplemented with 10 mM $MgCl_2$) and incubated at 37
587 °C for 1 hour. Beads were then washed with 50 µL TAPS wash buffer (10 mM TAPS pH 8.5, 0.2
588 mM EDTA), then resuspended in 5 µL TAPS wash buffer supplemented with 0.1% SDS and
589 incubated at 58 °C for 1 hour. SDS was neutralized on ice with 15 µL 0.67% Triton-X100. 2 µL
590 of 10 mM indexed P5 and P7 primer solutions and 25 µL NEBnext High-Fidelity 2X Master Mix
591 (New England BioLabs: ME541L) were added. Gap-filling and 15 cycles of PCR were performed
592 using an MJ PTC-200 Thermocycler. Library clean-up was performed by incubating beads with
593 65 µL SPRI bead slurry for 5-10 minutes, then magnetization and two washes with 200 µL 80%
594 ethanol. Libraries were eluted with 22 µL Tris-HCl pH 8.0 and 2 µL was used for Agilent 4200
595 Tapestation analysis. The barcoded libraries were mixed to achieve equimolar representation as

596 desired aiming for a final concentration as recommended by the manufacturer for sequencing
597 on an Illumina HiSeq 2500 2-lane Turbo flow cell.

598 **CUT&Tag data processing:**

599 CUT&Tag raw sequencing data were aligned to a custom genome made by concatenating
600 human (hg38), HSV (JN555585.1), and E. coli (U00096.3 Escherichia coli str. K-12 substr.
601 MG1655, complete genome). We performed alignments using bowtie2.

602 **Domain calling:**

603 Coverage at 100 bp windows of the human hg38 reference genome was calculated as number
604 of reads of given length (120-1000 bp for the analyses presented here) that mapped at that
605 window normalized by the factor N:

606 N= 10,000/(Total number of reads that mapped to E. coli genome)

607 Here 10,000 is an arbitrarily chosen number. We used *E. coli* DNA as a spike-in to normalize all
608 datasets. We partitioned all chromosomes into domains of macroH2A1: domains had an
609 enrichment that was two times the genome-wide median and at least four-fold higher than the
610 IgG control. The normalized coverage at each base-pair from each replicate was averaged
611 when combining multiple replicates. The normalized read density in 100 bp bins were then
612 smoothed with a running average over the bins spanning +/- 1000 bp around each bin. We then
613 calculated the genome-wide distribution of normalized read density and medians that were
614 plotted in Figure S1. We averaged medians across WT macroH2A1 datasets (mock, 4, 8, and
615 12hpi), and multiplied the average by 2, to set the cutoff for domain definition for macroH2A1
616 datasets. We defined a similar cutoff for H3K27me3 datasets using H3K27me3 WT datasets.

617 **Identifying domain level dynamics of macroH2A1 over time course of infection:**

618 To measure changes in macroH2A1 across time points where the domain boundaries are not
619 the same, we first concatenated domain definitions from all macroH2A1 datasets and then
620 defined a set of non-overlapping intervals using the “disjoin” method of GenomicRanges R
621 package [44]. We then calculated the log2 ratio of macroH2A1 enrichment over IgG for the non-
622 overlapping regions for the mock, 4, 8, and 12hpi. The 4, 8, and 12hpi enrichments were then
623 divided by the enrichment of the mock dataset to obtain change in macroH2A1 over time course
624 at the non-overlapping regions. k-means clustering (k=6) using R [45] was performed on the
625 matrix where the rows are the non-overlapping regions and the columns are change in
626 macroH2A1 over mock at 4, 8, and 12hpi. We extended the non-overlapping regions by 5 bp on
627 each end and then merged regions within each cluster using “reduce” method of

628 GenomicRanges, to obtain domains in each cluster. We recalculated change in macroH2A1 at
629 4, 8, and 12hpi over mock, which was used to plot heatmaps and boxplots shown in Figure 1
630 and Figure S1. H3K27me3 enrichment for WT and macroH2A1 KO cells was calculated at
631 clustered macroH2A1 domains. The unique code for this work can be found here:
632 https://doi.org/10.5281/zenodo.6783949

633 **RNA sequencing:**

634 Three biological replicates per time point were obtained from independent infections. Cells were
635 harvested at the indicated times post-infection by trypsinization, washed with PBS and
636 centrifuged at 5000 xg for 2 minutes. Pellets were lysed with TRIzol (Thermo Fisher: 15-596-
637 026) and total RNA was harvested according to manufacturer's instructions. RNAs were then
638 treated with DNase (Qiagen: 79254) on RNeasy columns (Qiagen: 74104) per manufacturer's
639 instructions. RNA was precipitated with 3 volumes ice-cold 96% ethanol, 1 volume 3 M sodium
640 acetate pH 5.5, and 1 µL glycogen (Thermo Fischer: R055) overnight at -80 °C. Precipitated
641 RNAs were pelleted at 15,000 xg and 4 °C for 30 minutes, washed with ice-cold 75% ethanol
642 and spun as above for 10 min. RNA was resuspended in nuclease-free water.

643 RNA was quantified by Nanodrop and integrity analyzed with the 4200 Tapestation Bioanalyzer
644 system (Agilent). 500 ng of total RNA with an RNA Integrity Number (RIN) greater than 9.5 were
645 used to prepare sequencing libraries with the TruSeq® Stranded mRNA Library Prep Kit
646 (Illumina: 20020594). Library concentrations were measured with Qubit dsDNA HS Assay Kit
647 (Thermo Fisher: Q32854) then analyzed with Agilent High Sensitivity D5000 ScreenTape
648 System and pooled. Libraries were sequenced with 100-bp paired-end reads on an Illumina
649 NovaSeq 6000 SP sequencer at the Fred Hutch Genomics Core Facility

650 **RNA/4sU-RNA/Hi-C data processing:**

651 Fastq files were filtered to exclude reads that didn't pass Illumina's base call quality threshold.
652 STAR v2.7.1 [46] with 2-pass mapping was used to align paired-end reads to a combined
653 reference of human genome build hg38 and HSV1 genome JN555585.1
654 (https://www.ncbi.nlm.nih.gov/nuccore/JN555585.1/). FastQC 0.11.9
655 (https://www.bioinformatics.babraham.ac.uk/projects/fastqc/) and RSeQC 4.0.0 [47] were used for
656 QC including insert fragment size, read quality, read duplication rates, gene body coverage and
657 read distribution in different genomic regions. FeatureCounts [48] in Subread 1.6.5 was used to
658 quantify gene-level expression by strand-specific paired-end read counting.

659 Gene annotation were based on GENCODE V31 (https://www.gencodegenes.org/human/) and
660 GCA_000859985.2_ViralProj15217 (https://www.ncbi.nlm.nih.gov/data-

661 hub/genome/GCF_000859985.2/). For HSV1, annotated genes were collapsed into non-
662 overlapping transcribed regions, e.g. X indicating a transcribed region unique to gene X, X:Y
663 indicating an overlapping transcribed region for genes X and Y, and so on.

664 Bioconductor package edgeR 3.26.8 [49] was used to detect differential gene expression between
665 sample groups. Genes with low expression were excluded by requiring at least one count per
666 million in at least N samples (N is equal to the number of samples in the smaller group). The
667 filtered expression matrix was normalized by TMM method
668 (https://genomebiology.biomedcentral.com/articles/10.1186/gb-2010-11-3-r25) and subject to
669 significance testing using quasi-likelihood pipeline implemented in edgeR. Genes were deemed
670 differentially expressed if fold changes were greater than 2 in either direction and Benjamini-
671 Hochberg adjusted p-values were less than 0.01.

672 The intervals representing start and end of each gene were intersected with clustered
673 macroH2A1 domains to obtain cluster assignments for genes. Intersection was performed using
674 "intersect" function of bedtools [50]. Genes that did not uniquely intersect with domains in a single
675 cluster were discarded. The cluster assignments for genes were used for plotting total RNA fold
676 changes in Figure 2. Reads per kilobase of transcript per million reads mapped (RPKM) values
677 for 4sU-RNA was obtained from GEO (GSE59717) and converted to transcripts per million
678 (TPM). The TPM values across two 4sU-RNA replicates for each condition was averaged and
679 box plots were generated similarly to total RNA.

680 For calculating eigenvector distributions, compartment wig file was downloaded from the
681 following link:

682 https://4dn-open-data-public.s3.amazonaws.com/fourfront-webprod/wfoutput/b543cbf4-ce54-
683 4d2d-8960-281528ff18a6/4DNFI342UZP1.bw

684 Regions from compartment file intersecting with each domain cluster were extracted and the
685 values were used for generating box plots shown in Figure 2D.

686 **Electron Microscopy:**

687 Cells were fixed in 2% paraformaldehyde and 2.5% glutaraldehyde in 0.1M sodium cacodylate
688 buffer (pH 7.3) at 4 °C. Fixed cells were rinsed briefly in 1% sucrose in 50mM cacodylate (pH
689 7.2), then postfixed on ice for 30 mins in a solution of 1% osmium (EM Sciences: RT19152) and
690 0.8% potassium ferricyanide in 50mM cacodylate (pH 7.2). Cell pellets were washed twice
691 briefly at 25 °C in 1% sucrose in 50mM cacodylate (pH 7.2), then washed in three changes of
692 50mM cacodylate (pH 7.2) for 5 min each. Cell pellets were treated with 0.2% tannic acid
693 (Sigma-Aldrich: 1401-55-4) in 50 mM cacodylate (pH 7.2) for 15 minutes at 25 °C, then rinsed

694 several times in water. Cells were dehydrated through a graded ethanol series and embedded
695 in Epon 12 resin (Ted Pella: 18010). 70nm thin sections were cut using an Ultracut UC7
696 ultramicrotome (Leica Mikrosysteme) and collected on 200 mesh formvar/carbon copper grids
697 (Ted Pella: 01800). Sections were stained with 2% aqueous uranyl acetate and Reynolds lead
698 citrate. Cell pellet sections were imaged using a Talos L120C microscope operated at 120kV
699 with a Ceta-16M (4096 x 4096) camera (ThermoFisher Scientific).

700 All data were collected at spot size 5 with a 100um C2 aperture and 70um objective aperture.
701 For quantification, nuclei were targeted at 1250x and manually circled. Autofocus was set to -
702 2.0um. Nuclei were then imaged at 11000x as a montage and stitched together automatically
703 using SerialEM (Nexperion Inc). Stitched maps were exported as uncompressed 16-bit tif files
704 for further analysis. For qualitative analysis, images were manually focused to -2.0um defocus
705 and then 20 1-second frames were collected and drift-corrected using Velox software (Thermo
706 Fisher Scientific, Eindhoven, NL). Final summed images were exported as 16-bit tif files and
707 cropped using ImageJ.

708 Image analysis pipelines for counting capsids and for measuring chromatin density at the
709 nuclear envelope were deployed in MATLAB R2020b. Scripts are available on the Fred Hutch
710 GitHub repository. Capsid pipeline follows three steps: 1- nuclear boundaries identification, 2-
711 capsid detection, 3- capsid classification. Nuclear boundaries were identified with user input, by
712 outlining a freehand contour of the nucleus of interest, from which a binary mask is extracted.
713 Capsid detection was performed on the median-filtered complement of the original image, using
714 a Circular Hough Transform based algorithm, with phase coding for radii estimation[51], and
715 search radius ranging from 10.6 to 31.7 nm. Capsids residing within the nuclear mask were then
716 counted and classified. Detected capsids were classified in three categories (Empty,
717 Intermediate and Full), depending on the distribution of the pixel grayscale intensities within the
718 capsids relative to a normal distribution.

719 Width of heterochromatin abutting the nuclear envelope was quantified by measuring the length
720 of the binarized chromatin from 1D intensity profiles along the normal of the nuclear perimeter,
721 sampled at every 10 perimeter pixels. Dense heterochromatin was binarized using global Otsu's
722 thresholding method applied to the background-corrected complement of the contrast-adjusted
723 original image. Noise from the binarized image was further reduced by applying a 2D order
724 statistic filter using the minimum value of a varying domain interactively defined by the user, with
725 default value of 8-by-8 pixels. The resulting heterochromatin density distribution was normalized
726 to the total length of the nucleus' perimeter.

727

728 **SUPPLEMENTAL FIGURES**

729

Supplemental Figure S1. Quantification of macroH2A1 and H3K27me3 enrichment on host and viral genomes during HSV-1 infection.

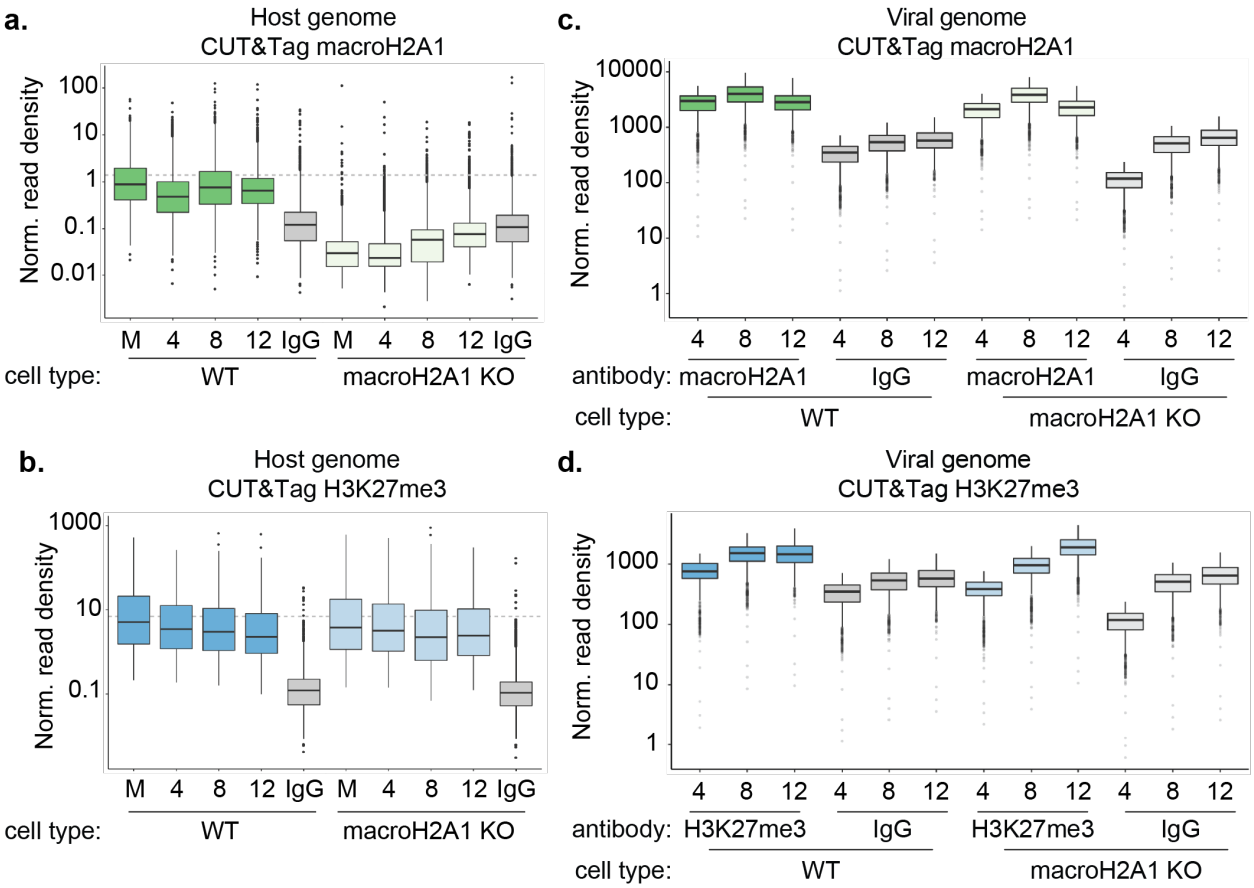

730

731 **Supplemental Figure S1. Quantification of macroH2A1 and H3K27me3 enrichment on**

732 **host and viral genomes during HSV-1 infection.**

733 a) Spike-in normalized CUT&Tag read density of macroH2A1 on WT HFF-T and

734 macroH2A1 KO cell genomes during HSV-1 infection.

735 b) Spike-in normalized CUT&Tag read density of H3K27me3 on WT HFF-T and

736 macroH2A1 KO cell genomes during HSV-1 infection.

737 c) Spike-in normalized CUT&Tag read density of macroH2A1 on HSV-1 genomes during

738 infection of WT HFF-T and macroH2A1 KO cells.

739 d) Spike-in normalized CUT&Tag read density of H3K27me3 on HSV-1 genomes during
740 infection of WT HFF-T and macroH2A1 KO cells.

741

Supplemental Figure S2. Quantification of macroH2A1 and H3K27me3 bound regions on host genomes during HSV-1 infection.

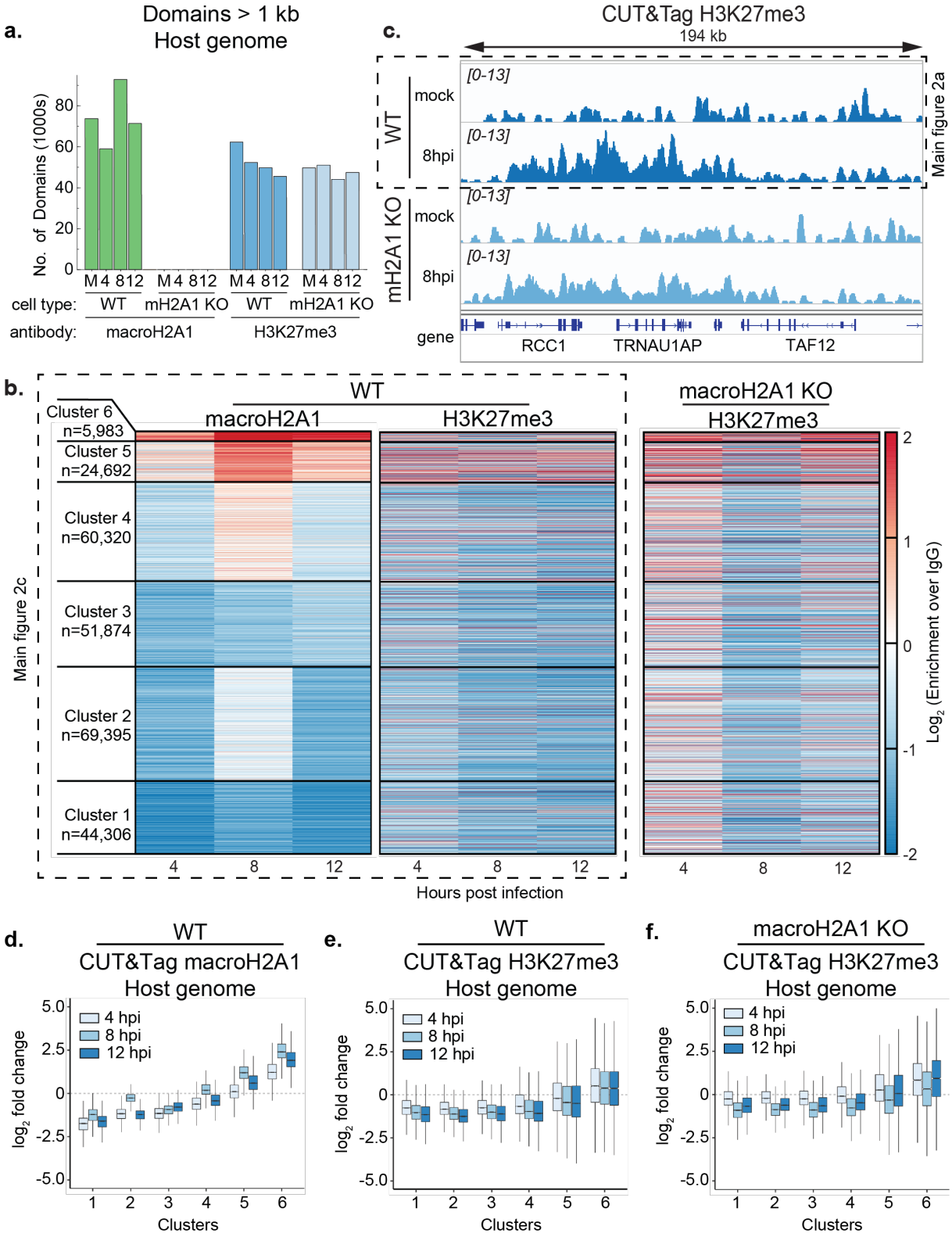

743 **Supplemental Figure S2. Quantification of macroH2A1 and H3K27me3 bound regions on**
744 **host genomes during HSV-1 infection.**

745 a) Total number of macroH2A1 and H3K27me3 domains over 1 kb as measured by
746 CUT&Tag of WT HFF-T and macroH2A1 KO cell genomes during HSV-1 infection.
747 b) Heat maps of macroH2A1 and H3K27me3 dynamics over the course of HSV-1 infection
748 generated from CUT&Tag data.
749 c) Representative screenshots of H3K27me3 broad domain increase over the course of
750 HSV-1 infection as measured by CUT&Tag.
751 d) Quantification of heat maps from Figure S2B showing macroH2A1 enrichment across
752 the clusters.
753 e) Quantification of heat maps from Figure S2B showing H3K27me3 enrichment in clusters
754 defined by macroH2A1 as in D.
755 f) Quantification as in E in macroH2A1 KO cells.

756
757
758

Supplemental Figure S3. MacroH2A1 and H3K27me3 presence on host genomes correlates with decreased transcription.

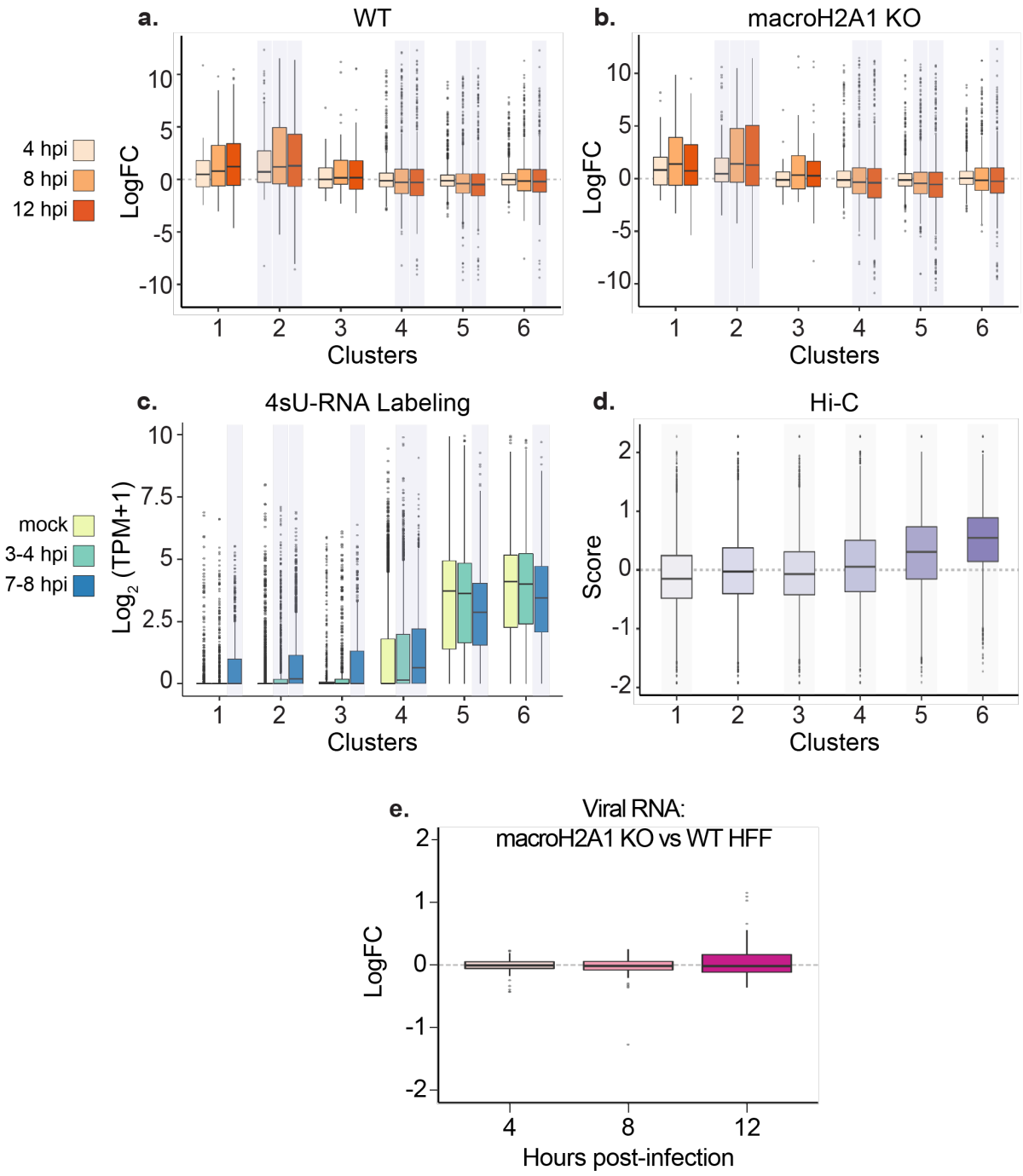

759

760

761

762 **Supplemental Figure S3. MacroH2A1 and H3K27me3 presence on host genomes**
763 **correlates with decreased transcription.**

764 a) Box plots of total host RNA from RNA-seq in HFF-T WT for genes overlapping clusters
765 from Figure 2. Kolmogrov-Smirnov test (in R) was performed comparing logCPM values
766 of genes at each time point with logCPM values of genes from mock dataset for each
767 cluster. The p-values were corrected for multiple testing, and the time points and clusters
768 with corrected p-value less than 0.05 are shaded.
769 b) Same as (a) for macroH2A1 KO cells.
770 c) 4sU-RNA counts for genes from Hennig *et al*[30] overlapping with clusters from Figure 2
771 shown as box plots and shading as indicated in (a).
772 d) Box plots of Hi-C eigenvector scores of regions overlapping with clusters from Figure 2.
773 The Hi-C compartment eigen vector scores were obtained from 4DN project website.
774 Wilcoxon signed rank test with alternate hypothesis that the true location is not equal to
775 0 was performed on the distribution of eigen vector scores for each cluster. The p-values
776 were corrected for multiple testing, and the clusters with corrected p-value less than 0.05
777 are shaded. Bonferroni correction was used for p-value adjustments.
778 e) Log2 fold-change of HSV-1 transcripts at 4, 8 and 12 hpi identified by RNA-seq in
779 macroH2A1 KO compared to WT HFF-T cells. There is no significant difference between
780 the cell types.

Supplemental Figure S4. Gene ontology enrichment analysis of total host mRNA defined by macroH2A1 clusters.

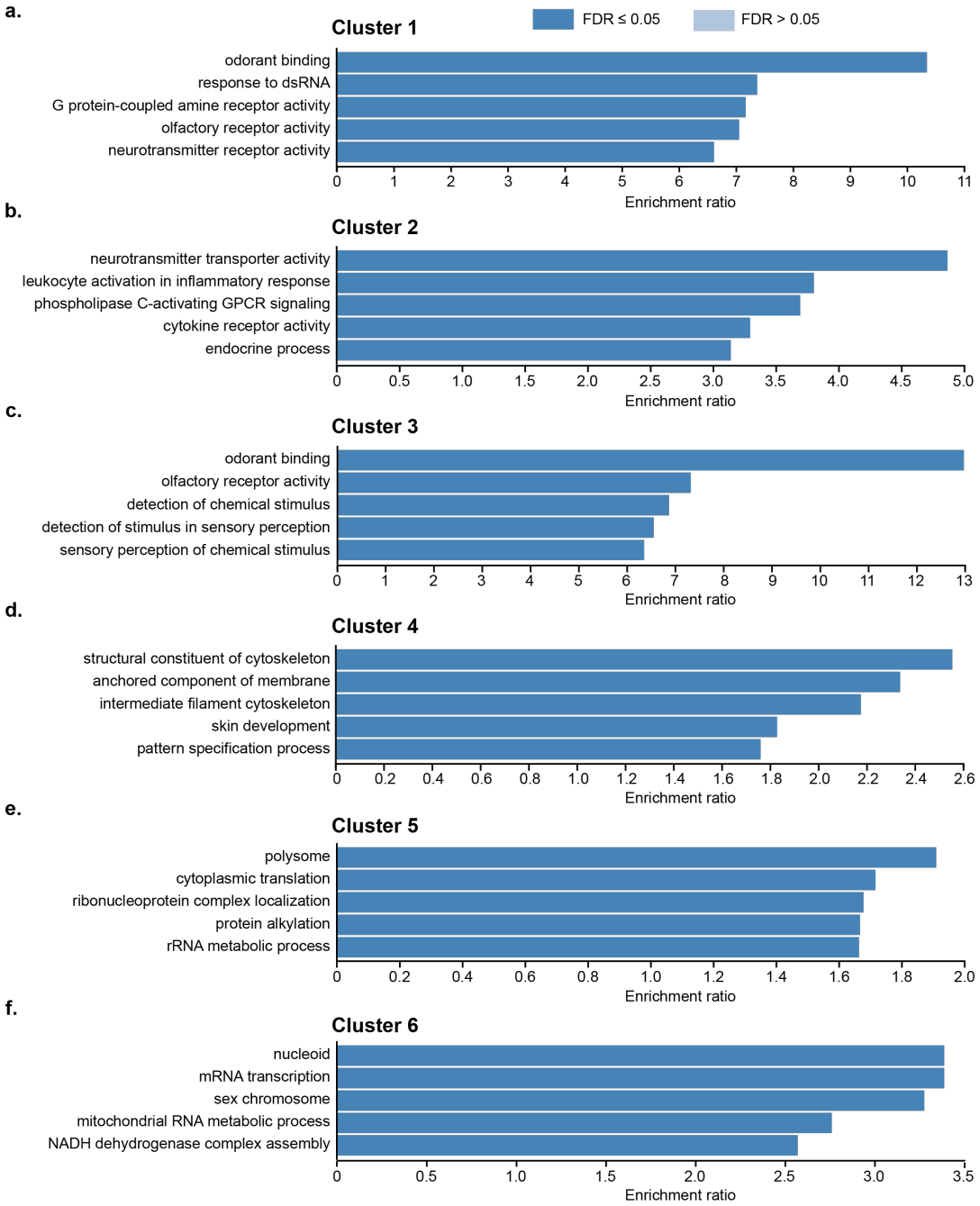

Supplemental Figure S4. Gene ontology enrichment analysis of total host mRNA defined by macroH2A1 clusters

Gene ontology analysis of mRNA levels between WT HFFs and macroH2A1 KO cells. Cluster 1 (a), cluster 2 (b), and cluster 3 (c), cluster 4 (d), cluster 5 (e), and cluster 6 (f) were defined by macroH2A1 domains in Figure 1. P-value <0.001 for all shown GO clusters and FDR was <0.05.

Supplemental Figure S5. Viral protein levels do not change upon macroH2A1 knockout or H3K27me3 depletion in HFFs and RPEs.

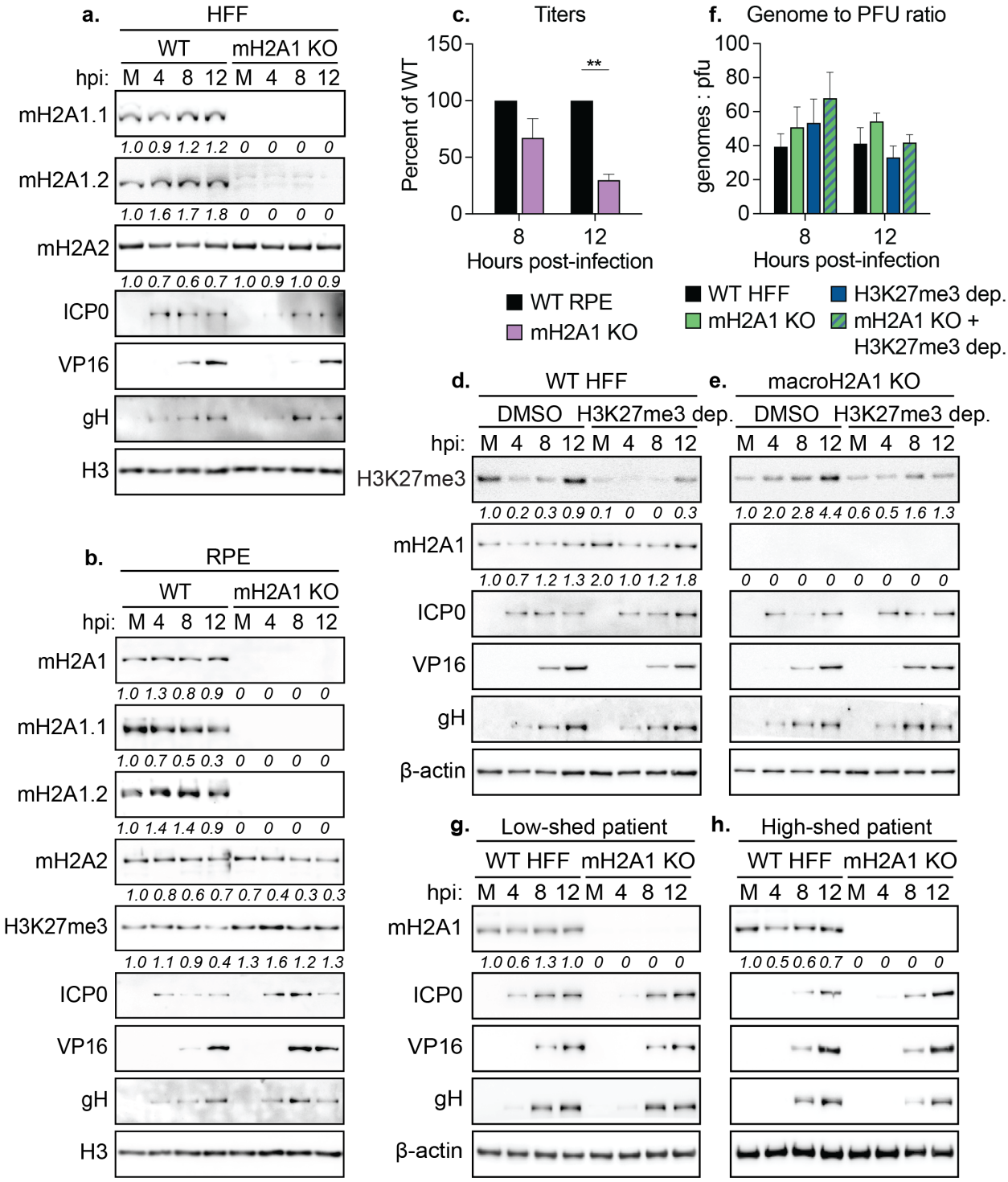

787

788 **Supplemental Figure S5. Viral protein levels do not change upon macroH2A1 knockout or**
789 **H3K27me3 depletion in HFFs and RPEs.**

790 a) Western blot of total macroH2A1, macroH2A1.1, and macroH2A1.2 isoforms and
791 macroH2A2 in mock(M) or during HSV-1 infection at 4-, 8-, and 12-hpi in WT and
792 macroH2A1 KO HFF-T cells. H3 is shown as a loading control. Quantification of relative
793 intensity over H3 normalized to the mock samples are shown.
794 b) Western blot as in (a) in WT and macroH2A1 KO tert-immortalized RPE cells. H3 is
795 shown as a loading control.
796 c) Infectious progeny produced by WT or macroH2A1 knockout RPE cells quantified by
797 plaque assay. Viral yield calculated as in Fig 3c for conditions as indicated, *** p. <
798 0.001.
799 d) Western blot of H3K27me3 and macroH2A1 during HSV-1 infection shown as mock
800 infected (M), 4-, 8-, and 12-hpi. WT cells H3K27me3 depleted or treated with DMSO for
801 3 days prior to infection and remained with inhibitor over the course of infection. Beta-
802 actin is shown as a loading control. Quantification of relative intensity over beta-actin
803 normalized to the mock sample on the same blot are shown.
804 e) Western blot as in (d) for macroH2A1 KO cells.
805 f) Western blots as in (a) for infections with low-shedding clinical isolate of HSV-1. Fold-
806 change of macroH2A1 protein levels normalized to macroH2A1 level in mock-infected
807 cells.
808 g) Western blot as in (f) for high-shedding clinical HSV-1 isolate.

Supplemental Figure S6. HSV-1 capsid formation is independent of macroH2A1 and H2K37me3.

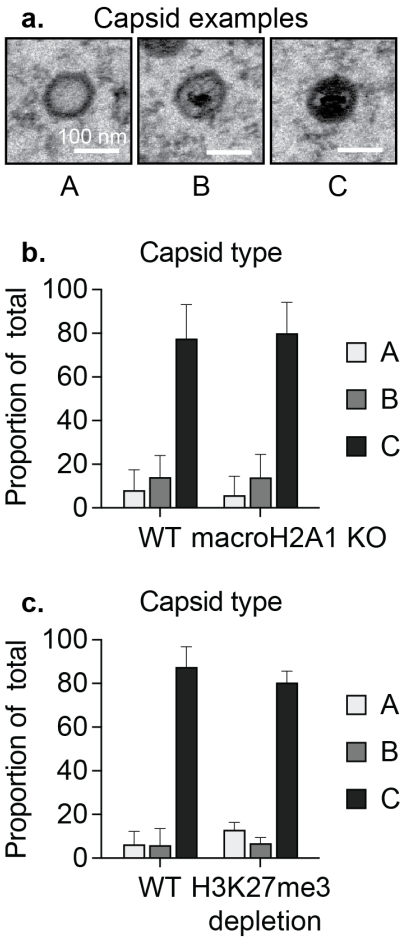

Supplemental Figure S6. HSV-1 capsid formation is independent of macroH2A1.

a) TEM images of representative A (empty), B (scaffolding proteins, but no genome), and C (full) HSV-1 capsids. Scale bars as noted for all TEM images.
b) Quantification of capsid type within nuclei from (a) in WT and macroH2A1 KO cells. Values for each capsid type are shown as a proportion of total capsids. No significance by ANOVA.
c) Capsid type quantification as in (b) for H3K27me3 depleted cells.

819 **REFERENCES CITED**

820

821 1. Knipe, D. M. & Cliffe, A. Chromatin control of herpes simplex virus lytic and latent infection. *Nat Rev*
822 *Microbiol* 6, 211–221 (2008).

823 2. Monier, K., Armas, J. C. G., Etteldorf, S., Ghazal, P. & Sullivan, K. F. Annexation of the
824 interchromosomal space during viral infection. *Nat Cell Biol* 2, 661–665 (2000).

825 3. Kulej, K., Avgousti, D. C., Sidoli, S., Herrmann, C., Fera, A. N. D., Kim, E. T., Garcia, B. A. &
826 Weitzman, M. D. Time-resolved Global and Chromatin Proteomics during Herpes Simplex Virus Type 1
827 (HSV-1) Infection. *Mol Cell Proteomics* 16, S92–S107 (2017).

828 4. Aho, V., Mäntylä, E., Ekman, A., Hakanen, S., Mattola, S., Chen, J.-H., Weinhardt, V., Ruokolainen,
829 V., Sodeik, B., Larabell, C. & Vihinen-Ranta, M. Quantitative Microscopy Reveals Stepwise Alteration
830 of Chromatin Structure during Herpesvirus Infection. *Viruses* 11, 935 (2019).

831 5. Aho, V., Salminen, S., Mattola, S., Gupta, A., Flomm, F., Sodeik, B., Bosse, J. B. & Vihinen-Ranta, M.
832 Infection-induced chromatin modifications facilitate translocation of herpes simplex virus capsids to the
833 inner nuclear membrane. *Plos Pathog* 17, e1010132 (2021).

834 6. Roller, R. J. & Johnson, D. C. Herpesvirus Nuclear Egress across the Outer Nuclear Membrane.
835 *Viruses* 13, 2356 (2021).

836 7. Arii, J. Host and Viral Factors Involved in Nuclear Egress of Herpes Simplex Virus 1. *Viruses* 13, 754
837 (2021).

838 8. Myllys, M., Ruokolainen, V., Aho, V., Smith, E. A., Hakanen, S., Peri, P., Salvetti, A., Timonen, J.,
839 Hukkanen, V., Larabell, C. A. & Vihinen-Ranta, M. Herpes simplex virus 1 induces egress channels
840 through marginalized host chromatin. *Sci Rep-uk* 6, 28844 (2016).

841 9. Chi, P., Allis, C. D. & Wang, G. G. Covalent histone modifications — miswritten, misinterpreted and
842 mis-erased in human cancers. *Nat Rev Cancer* 10, 457–469 (2010).

843 10. Margueron, R. & Reinberg, D. The Polycomb complex PRC2 and its mark in life. *Nature* 469, 343–
844 349 (2011).

845 11. Gamble, M. J. & Kraus, W. L. Multiple facets of the unique histone variant macroH2A: From
846 genomics to cell biology. *Cell Cycle* 9, 2568–2574 (2010).

847 12. Kapoor, A., Goldberg, M. S., Cumberland, L. K., Ratnakumar, K., Segura, M. F., Emanuel, P. O.,
848 Menendez, S., Vardabasso, C., LeRoy, G., Vidal, C. I., Polsky, D., Osman, I., Garcia, B. A., Hernando, E.
849 & Bernstein, E. The histone variant macroH2A suppresses melanoma progression through regulation of
850 CDK8. *Nature* 468, 1105–1109 (2010).

851 13. Douet, J., Corujo, D., Malinverni, R., Renauld, J., Sansoni, V., Marjanović, M. P., Cantariño, N.,
852 Valero, V., Mongelard, F., Bouvet, P., Imhof, A., Thiry, M. & Buschbeck, M. MacroH2A histone variants
853 maintain nuclear organization and heterochromatin architecture. *J Cell Sci* 130, 1570–1582 (2017).

854 14. Fu, Y., Lv, P., Yan, G., Fan, H., Cheng, L., Zhang, F., Dang, Y., Wu, H. & Wen, B. MacroH2A1
855 associates with nuclear lamina and maintains chromatin architecture in mouse liver cells. *Sci Rep-uk* 5,
856 17186 (2015).

857 15. Spear, P. G. Herpes simplex virus: receptors and ligands for cell entry. *Cell Microbiol* 6, 401–410
858 (2004).

859 16. Aho, V., Myllys, M., Ruokolainen, V., Hakanen, S., Mäntylä, E., Virtanen, J., Hukkanen, V., Kühn,
860 T., Timonen, J., Mattila, K., Larabell, C. A. & Vihinen-Ranta, M. Chromatin organization regulates viral
861 egress dynamics. *Sci Rep-uk* 7, 3692 (2017).

862 17. Ghiraldini, F. G., Filipescu, D. & Bernstein, E. Solid tumours hijack the histone variant network. *Nat*
863 *Rev Cancer* 21, 257–275 (2021).

864 18. Rickels, R., Hu, D., Collings, C. K., Woodfin, A. R., Piunti, A., Mohan, M., Herz, H.-M., Kvon, E. &
865 Shilatifard, A. An Evolutionary Conserved Epigenetic Mark of Polycomb Response Elements
866 Implemented by Trx/MLL/COMPASS. *Mol Cell* 63, 318–328 (2016).

867 19. Lue, J. K. & Amengual, J. E. Emerging EZH2 Inhibitors and Their Application in Lymphoma. *Curr*
868 *Hematol Malig R* 13, 369–382 (2018).

869 20. Kaya-Okur, H. S., Wu, S. J., Codomo, C. A., Pledger, E. S., Bryson, T. D., Henikoff, J. G., Ahmad,
870 K. & Henikoff, S. CUT&Tag for efficient epigenomic profiling of small samples and single cells. *Nat*
871 *Commun* 10, 1930 (2019).

872 21. Friedel, C. C., Whisnant, A. W., Djakovic, L., Rutkowski, A. J., Friedl, M.-S., Kluge, M.,
873 Williamson, J. C., Sai, S., Vidal, R. O., Sauer, S., Hennig, T., Grothey, A., Milić, A., Prusty, B. K.,
874 Lehner, P. J., Matheson, N. J., Erhard, F. & Dölken, L. Dissecting Herpes Simplex Virus 1-Induced Host
875 Shutoff at the RNA Level. *J Virol* 95, e01399-20 (2021).

876 22. Lieberman-Aiden, E., Berkum, N. L. van, Williams, L., Imakaev, M., Ragoczy, T., Telling, A., Amit,
877 I., Lajoie, B. R., Sabo, P. J., Dorschner, M. O., Sandstrom, R., Bernstein, B., Bender, M. A., Groudine,
878 M., Gnirke, A., Stamatoyannopoulos, J., Mirny, L. A., Lander, E. S. & Dekker, J. Comprehensive
879 Mapping of Long-Range Interactions Reveals Folding Principles of the Human Genome. *Science* 326,
880 289–293 (2009).

881 23. Rao, S. S. P., Huntley, M. H., Durand, N. C., Stamenova, E. K., Bochkov, I. D., Robinson, J. T.,
882 Sanborn, A. L., Machol, I., Omer, A. D., Lander, E. S. & Aiden, E. L. A 3D Map of the Human Genome
883 at Kilobase Resolution Reveals Principles of Chromatin Looping. *Cell* 159, 1665–1680 (2014).

884 24. Cai, W. & Schaffer, P. A. Herpes simplex virus type 1 ICP0 regulates expression of immediate-early,
885 early, and late genes in productively infected cells. *J Virol* 66, 2904–2915 (1992).

886 25. Naldinho-Souto, R., Browne, H. & Minson, T. Herpes Simplex Virus Tegument Protein VP16 Is a
887 Component of Primary Enveloped Virions. *J Virol* 80, 2582–2584 (2006).

888 26. Lorentzen, E. U., Eing, B. R., Hafezi, W., Manservigi, R. & Kühn, J. E. Replication-Competent
889 Herpes simplex Virus Type 1 Mutant Expressing an Autofluorescent Glycoprotein H Fusion Protein.
890 *Intervirology* 44, 232–242 (2001).

891 27. Arbuckle, J. H., Gardina, P. J., Gordon, D. N., Hickman, H. D., Yewdell, J. W., Pierson, T. C., Myers,
892 T. G. & Kristie, T. M. Inhibitors of the Histone Methyltransferases EZH2/1 Induce a Potent Antiviral
893 State and Suppress Infection by Diverse Viral Pathogens. *Mbio* 8, e01141-17 (2017).

894 28. Gibson, W. & Roizman, B. Proteins Specified by Herpes Simplex Virus VIII. Characterization and
895 Composition of Multiple Capsid Forms of Subtypes 1 and 2. *J Virol* 10, 1044–1052 (1972).

896 29. Yu, X.-K., O'Connor, C. M., Atanasov, I., Damania, B., Kedes, D. H. & Zhou, Z. H. Three-
897 Dimensional Structures of the A, B, and CCapsids of Rhesus Monkey Rhadinovirus: Insights into
898 GammaherpesvirusCapsid Assembly, Maturation, and DNAPackaging. *J Virol* 77, 13182–13193 (2003).

899 30. Hennig, T., Michalski, M., Rutkowski, A. J., Djakovic, L., Whisnant, A. W., Friedl, M.-S., Jha, B. A.,
900 Baptista, M. A. P., L'Hernault, A., Erhard, F., Dölken, L. & Friedel, C. C. HSV-1-induced disruption of
901 transcription termination resembles a cellular stress response but selectively increases chromatin
902 accessibility downstream of genes. *Plos Pathog* 14, e1006954 (2018).

903 31. Bjerke, S. L. & Roller, R. J. Roles for herpes simplex virus type 1 UL34 and US3 proteins in
904 disrupting the nuclear lamina during herpes simplex virus type 1 egress. *Virology* 347, 261–276 (2006).

905 32. Simpson-Holley, M., Baines, J., Roller, R. & Knipe, D. M. Herpes Simplex Virus 1 UL31 and UL34
906 Gene Products Promote the Late Maturation of Viral Replication Compartments to the Nuclear Periphery.
907 *J Virol* 78, 5591–5600 (2004).

908 33. Leach, N. R. & Roller, R. J. Significance of host cell kinases in herpes simplex virus type 1 egress and
909 lamin-associated protein disassembly from the nuclear lamina. *Virology* 406, 127–137 (2010).

910 34. Bahnamiri, M. M. & Roller, R. J. Mechanism of Nuclear Lamina Disruption and the Role of pUS3 in
911 Herpes Simplex Virus 1 Nuclear Egress. *J Virol* 95, (2021).

912 35. Bigalke, J. M., Heuser, T., Nicastro, D. & Heldwein, E. E. Membrane deformation and scission by the
913 HSV-1 nuclear egress complex. *Nat Commun* 5, 4131–4131 (2014).

914 36. Draganova, E. B., Thorsen, M. K. & Heldwein, E. E. Nuclear Egress of Herpesviruses. *Curr Issues*
915 *Mol Biol* 41, 125–170 (2021).

916 37. Lynch, K. L., Dillon, M. R., Bat-Erdene, M., Lewis, H. C., Kaai, R. J., Arnold, E. A. & Avgousti, D.
917 C. A viral histone-like protein exploits antagonism between linker histones and HMGB proteins to
918 obstruct the cell cycle. *Curr Biol* (2021). doi:10.1016/j.cub.2021.09.050

919 38. Brown, S. M., Ritchie, D. A. & Subak-Sharpe, J. H. Genetic Studies with Herpes Simplex Virus Type
920 1. The Isolation of Temperature-sensitive Mutants, their Arrangement into Complementation Groups and
921 Recombination Analysis Leading to a Linkage Map. *J Gen Virol* 18, 329–346 (1973).

922 39. Lilley, C. E., Carson, C. T., Muotri, A. R., Gage, F. H. & Weitzman, M. D. DNA repair proteins
923 affect the lifecycle of herpes simplex virus 1. *P Natl Acad Sci Usa* 102, 5844–5849 (2005).

924 40. Hatch, E. M., Kulukian, A., Holland, A. J., Cleveland, D. W. & Stearns, T. Cep152 interacts with
925 Plk4 and is required for centriole duplication. *J Cell Biol* 191, 721–729 (2010).

926 41. Li, G., Nguyen, C. C., Ryckman, B. J., Britt, W. J. & Kamil, J. P. A viral regulator of glycoprotein
927 complexes contributes to human cytomegalovirus cell tropism. *Proc National Acad Sci* 112, 4471–4476
928 (2015).

929 42. Child, S. J., Greninger, A. L. & Geballe, A. P. Rapid adaptation to human protein kinase R by a
930 unique genomic rearrangement in rhesus cytomegalovirus. *Plos Pathog* 17, e1009088 (2021).

931 43. Aubert, M., Boyle, N. M., Stone, D., Stensland, L., Huang, M.-L., Magaret, A. S., Galetto, R.,
932 Rawlings, D. J., Scharenberg, A. M. & Jerome, K. R. In vitro Inactivation of Latent HSV by Targeted
933 Mutagenesis Using an HSV-specific Homing Endonuclease. *Mol Ther Nucleic Acids* 3, e146 (2014).

934 44. Lawrence, M., Huber, W., Pagès, H., Aboyoun, P., Carlson, M., Gentleman, R., Morgan, M. T. &
935 Carey, V. J. Software for Computing and Annotating Genomic Ranges. *Plos Comput Biol* 9, e1003118
936 (2013).

937 45. Team, R. C. R: A Language and Environment for Statistical Computing. *R Foundation for Statistical*
938 *Computing* (2019). at <https://www.R-project.org>

939 46. Dobin, A., Davis, C. A., Schlesinger, F., Drenkow, J., Zaleski, C., Jha, S., Batut, P., Chaisson, M. &
940 Gingeras, T. R. STAR: ultrafast universal RNA-seq aligner. *Bioinformatics* 29, 15–21 (2013).

941 47. Wang, L., Wang, S. & Li, W. RSeQC: quality control of RNA-seq experiments. *Bioinformatics* 28,
942 2184–2185 (2012).

943 48. Liao, Y., Smyth, G. K. & Shi, W. featureCounts: an efficient general purpose program for assigning
944 sequence reads to genomic features. *Bioinformatics* 30, 923–930 (2014).

945 49. Robinson, M. D., McCarthy, D. J. & Smyth, G. K. edgeR: a Bioconductor package for differential
946 expression analysis of digital gene expression data. *Bioinformatics* 26, 139–140 (2010).

947 50. Quinlan, A. R. & Hall, I. M. BEDTools: a flexible suite of utilities for comparing genomic features.
948 *Bioinformatics* 26, 841–842 (2010).

949 51. Atherton, T. J. & Kerbyson, D. J. Size invariant circle detection. *Image Vision Comput* 17, 795–803
950 (1999).

951